

# Development of Fe<sub>3</sub>O<sub>4</sub> core-TiO<sub>2</sub> shell nanocomposites and nanoconjugates as a foundation for neuroblastoma radiosensitization

**William Liu**

Northwestern University

**Salida Mirzoeva**

Northwest University

**Ye Yuan**

Northwestern University

**Junjing Deng**

Argonne National Laboratory

**Si Chen**

Argonne National Laboratory

**Barry Lai**

Argonne National Laboratory

**Stefan Vogt**

Argonne National Laboratory

**Karna Shah**

Northwestern University

**Rahul Shroff**

Northwestern University

**Reiner Bleher**

Northwestern University

**Qiaoling Jin**

Argonne National Laboratory

**Nghia Vo**

Diamond Light Source Ltd

**Remon Bazak**

Alexandria University Faculty of Medicine

**Carissa Ritner**

Northwestern University

**Stanley Gutionov**

Northwestern University

**Sumita Raha**

Northwestern University

**Julia Sedlmair**

National Synchrotron Radiation Research Center

**Carol Hirschmugl**

University of Wisconsin Milwaukee

**Chris Jacobsen**

Argonne National Laboratory

**Tatjana Paunesku**

Northwestern University

**John Kalapurkal**

Northwest University

**Gayle Woloschak (✉ [gayle.woloschak@gmail.com](mailto:gayle.woloschak@gmail.com))**

Northwestern University <https://orcid.org/0000-0001-9209-8954>

---

**Research**

**Keywords:** Nanocomposites, Nanoconjugates, iron oxide core nanoparticles, titanium dioxide shell nanoparticles, neuroblastoma, radiosensitization

**Posted Date:** September 4th, 2020

**DOI:** <https://doi.org/10.21203/rs.3.rs-53387/v1>

**License:**  This work is licensed under a Creative Commons Attribution 4.0 International License.

[Read Full License](#)

---

**Version of Record:** A version of this preprint was published at Cancer Nanotechnology on May 14th, 2021. See the published version at <https://doi.org/10.1186/s12645-021-00081-z>.

# **Abstract**

## **Background**

Neuroblastoma is the most common extracranial solid malignancy in childhood which, despite the current progress in radiotherapy and chemotherapy protocols, still has a high mortality rate in high risk tumors. Nanomedicine offers exciting and unexploited opportunities to overcome the shortcomings of conventional medicine. The photocatalytic properties of  $\text{Fe}_3\text{O}_4$  core- $\text{TiO}_2$  shell nanocomposites and their potential for cell specific targeting suggest that nanoconstructs produced using  $\text{Fe}_3\text{O}_4$  core- $\text{TiO}_2$  shell nanocomposites could be used to enhance radiation effects in neuroblastoma. In this study, we evaluated bare, metaiodobenzylguanidine (MIBG) and 3,4-Dihydroxyphenylacetic acid (DOPAC) coated  $\text{Fe}_3\text{O}_4@\text{TiO}_2$  as potential radiosensitizers for neuroblastoma *in vitro*.

## **Results**

The uptake of bare and MIBG coated nanocomposites modestly sensitized neuroblastoma cells to ionizing radiation. Conversely, cells exposed to DOPAC coated nanocomposites exhibited a five-fold enhanced sensitivity to radiation, increased numbers of radiation induced DNA double-strand breaks, and apoptotic cell death. The addition of a peptide mimic of the epidermal growth factor (EGF) to nanoconjugates coated with MIBG altered their intracellular distribution. Cryo X-ray fluorescence microscopy tomography of frozen hydrated cells treated with these nanoconjugates revealed cytoplasmic as well as nuclear distribution of the nanoconstructs.

## **Conclusions**

The intracellular distribution pattern of different nanoconjugates used in this study was different for different nanoconjugate surface molecules. Cells exposed to DOPAC covered nanoconjugates showed the smallest nanoconjugate uptake, with the most prominent pattern of large intracellular aggregates. Interestingly, cells treated with this nanoconjugate also showed the most pronounced radiosensitization effect in combination with the external beam x-ray irradiation. Further studies are necessary to evaluate mechanistic basis for this increased radiosensitization effect. Preliminary studies with the nanoparticles carrying an EGF mimicking peptide showed that this approach to targeting could perhaps be combined with a different approach to radiosensitization – use of nanoconjugates in combination with the radioactive iodine. Much additional work will be necessary in order to evaluate possible benefits of targeted nanoconjugates carrying radionuclides.

# **Background**

Neuroblastoma is the most common extracranial solid malignancy among children under 15 years of age.(Baade et al. 2010 20051948; Chen et al. 2014 24365918; Gatta et al. 2012 22357215; Kacar et al. 2013 22105573; Stiller 2004 15322515; Ward et al. 2014 24488779) It arises within the sympathetic nervous system from primordial neural crest cells of sympatheticoadrenal lineage. Neuroblastoma is a

heterogeneous tumor with a highly variable clinical behavior. Although low- to intermediate-risk tumors tend to have a favorable prognosis, high-risk tumors often exhibit less than 50% overall survival rate. (Maris et al. 2007 17586306) The variable clinical outcome, which mounts to inexorable progression despite intensive therapy, reflects the genetic heterogeneity of these tumors. (Aygun 2018 29380702) The most consistent genetic abnormality associated with adverse outcomes is genomic amplification of N-myc proto-oncogene protein (MYCN), which occurs in nearly 20% of primary tumors (Maris et al. 2007 17586306) Neuroblastoma is notorious for relapse, which occurs in up to 60% of cases and is often refractive to most currently available treatment modalities. (Maris 2010 20558371) Primary neuroblastomas often have a wild type p53 which in combination with MYCN, often results in treatment induced apoptosis (Yoshida 2018 30053872). However, upon relapse, neuroblastomas become p53 negative which renders these tumors resistant to therapy. (Huang and Weiss 2013 24086065) Gene sequencing of neuroblastoma samples has revealed that the genetic makeup of up to 78% of relapsed neuroblastomas harbors new genetic mutations in the RAS-Mitogen-activated protein kinase pathway (RAS-MAPK) and novel MYCN amplifications. (Eleveld et al. 2015 26121087; Schramm et al. 2015 26121086) The current standard of care for neuroblastoma entails multiple treatment modalities, all of which have a deleterious effect on health.(Maris 2010 20558371) Even targeted therapies such as radioactive metaiodobenzylguanidine (MIBG) carry with it numerous treatment related hurdles ranging from myelosuppression as the dose-limiting toxicity, to difficulties in isolating young radio-iodine treated children essential for protection of caregivers. (DuBois and Matthay 2008 18707633; Matthay et al. 2012 22589483; Matthay et al. 2007 17369569) New approaches with targeted therapies are under investigation; however, few are as efficient for relapsed neuroblastoma as radioactive MIBG.

Nanotechnology provides a myriad of encouraging targeting opportunities to tackle current limitations in conventional treatment modalities. (Bazak et al. 2014 25279172; Bazak et al. 2015 25005786)  $\text{Fe}_3\text{O}_4$  core- $\text{TiO}_2$  shell ( $\text{Fe}_3\text{O}_4@\text{TiO}_2$ ) nanocomposites are unique in having surface reactivity and photocatalytic properties that render them an attractive platform for inducing controlled targeted cytotoxicity and DNA scission in neoplastic cells. (Bazak et al. 2013 23824281; Yuan et al. 2013 24219664) The photocatalytic properties of  $\text{Fe}_3\text{O}_4@\text{TiO}_2$  nanocomposites is based on the ability of  $\text{TiO}_2$  shell to produce reactive oxygen species (ROS) when exposed to photons with energies greater than 3.2 eV (Blake et al. 1999). These ROS interact with adjacent intracellular substructures to induce direct Deoxyribonucleic Acid (DNA) damage, (Cooke et al. 2003 12832285) mitochondrial ROS-induced ROS release, (Zorov et al. 2006 16829228) and ultimately cell death. (Ryter et al. 2007 17115887) Owing to the unique physico-chemical characteristics of  $\text{Fe}_3\text{O}_4@\text{TiO}_2$  nanocomposites, they have been explored in several contexts. Arora and others (Arora et al. 2012 22158944) utilized  $\text{Fe}_3\text{O}_4@\text{TiO}_2$  nanoconstructs for intracellular delivery of doxorubicin circumventing drug resistance in ovarian cancer cell lines. Bazak et al. (Bazak et al. 2013 23824281) and Yuan et al. (Yuan et al. 2013 24219664) have targeted  $\text{Fe}_3\text{O}_4@\text{TiO}_2$  to the nucleus of nasal and cervical cancer cell lines, and achieved light induced genomic DNA degradation. The versatile capabilities of  $\text{Fe}_3\text{O}_4@\text{TiO}_2$  for active targeting coupled with controlled induction of cytotoxicity in neoplastic cells render these nanoconstructs a platform worth exploring for management of neuroblastoma.

In this study, we investigated whether bare and surface modified  $\text{Fe}_3\text{O}_4@\text{TiO}_2$  nanocomposites can enhance radiation induced ROS production in four genetically distinct neuroblastoma cell lines. The SK-N-AS cell line has a mutated NRAS gene, a non-functional p53, and a single copy of MYCN. In contrast, SK-N-DZ cell line harbors a wild type p53 (Nakamura et al. 2007 17276397) but with an amplified MYCN. Both NBL-W/S and NBL-W/N cell lines have about 100 copies of the MYCN gene; (Foley et al. 1991 1933896) nevertheless, N-myc protein in NBL-W/S cells is 10-fold less than in NBL-W/N due to differences in MYCN mRNA stability.(Chagnovich and Cohn 1997 9516853) The cell lines used in this study are morphologically of the neuroblastic and substrate adherent phenotypes. Primary neuroblastoma is a heterogenous tumor and generally harbors cells of both phenotypes.(Kim et al. 2004 14712218) We chose to work with a diverse set of neuroblastoma cell lines in order to observe relative differences in treatment efficiency of nanocomposites under investigation, reflecting the genetic and physiological diversity seen in the clinic. Some of the work, however, was conducted only on SK-N-AS cell line because these cells share many critical aspects of refractory neuroblastoma such as non-functional p53 and mutated NRAS gene. (Eleveld et al. 2015 26121087)

Neuroblastoma cell lines have been used as a model for investigation of dopamine uptake and synthesis (Cooke et al. 2003 12832285) and dopaminergic neuroblastoma has been associated with a poor clinical outcome. (Nakagawara et al. 1988 3385588) Therefore, we explored 3,4-Dihydroxyphenylacetic acid (DOPAC) as a possible coating for  $\text{Fe}_3\text{O}_4@\text{TiO}_2$  nanocomposites. We have previously used dopamine and DOPAC to conjugate small molecules to nanocomposite surfaces; (Arora et al. 2012 22158944; Bazak et al. 2013 23824281; Brown et al. 2018 29541425; Chen et al. 2014 24365918; Paunesku et al. 2003 12692534; Paunesku et al. 2007 17274661; Yuan et al. 2013 24219664) however, in this study DOPAC itself was designated to serve as nanocomposite surface modification as well as anchor for conjugation of MIBG.

## Results

### Modification of nanocomposite surface coating affects size, aggregation, and cellular uptake

We examined how the coating of nanocomposites with DOPAC or DOPAC conjugated to MIBG might affect nanoconjugate physical characteristics. Measurements of zeta potentials of these nanoconstructs are shown in Supplemental Table 1. It should be noted that MIBG was conjugated to  $\text{Fe}_3\text{O}_4@\text{TiO}_2$  nanocomposites via a DOPAC linker through a reaction using 1-ethyl-3-(3-dimethylaminopropyl) carbodiimide hydrochloride (EDC) and with MIBG as the molecule in higher excess. Under these conditions, no free COOH groups of DOPAC remained on the nanoconjugate surface. We refer to those nanoconjugates as MIBG coated although it is DOPAC that provides a covalent link between nanoconstruct surface and MIBG (see Supplemental Figs. 1 and 2). These nanocomposites were imaged by Energy Dispersive Spectroscopy (EDS) – Scanning Transmission Electron Microscopy (STEM) (Supplemental Fig. 1), and elemental maps were generated. There was a clear overlap between iodine (I),

iron (Fe), and titanium (Ti) in the elemental map images seen in Supplemental Fig. 1b, indicating the successful binding of MIBG to the surface of the nanocomposite. Progression through chemical changes on the surface of the nanocomposites correlated with nanoparticle coating was also confirmed by imaging with infrared spectroscopy (Supplemental Fig. 2).

Bare, DOPAC and MIBG conjugated nanocomposites were suspended in serum-containing DMEM and drop cast onto lacey-carbon grids for Transmission Electron Microscopy (TEM), plunge frozen, and imaged under cryogenic conditions (Fig. 1a-c). We observed a difference in size and aggregation properties of the different nanoconstructs under these conditions. In complete medium, aggregates formed from bare nanocomposites were much smaller than aggregates of DOPAC coated nanoconjugates. MIBG coated nanoconjugates were similar in size and aggregation to the bare nanocomposites. It is possible that the highly polar surface of DOPAC coated nanoconjugates, with numerous electronegative carboxyl groups exposed to the medium, led to cooperative binding to electropositive components in complete medium and aggregation of nanoconjugates, while bare and MIBG coated nanoconstructs acquired only a single layer of protein corona.

We then examined cellular uptake of bare, DOPAC and MIBG coated nanoconstructs by inductively coupled plasma mass spectrometry (ICP-MS) (Fig. 1d-e). When neuroblastoma cells (SK-N-AS and SK-N-DZ) were treated for 1 hour with equivalent concentrations of  $\text{Fe}_3\text{O}_4@\text{TiO}_2$  nanocomposites (250 nM), there was significantly less uptake of DOPAC-coated nanoconjugates when compared to either bare nanocomposites or MIBG coated nanoconjugates in both cell lines. This could be explained by the observed difference in aggregation properties of the nanoconstructs. The observed size of bare and MIBG coated nanoparticles aggregates imaged by TEM was much smaller compared to aggregates of DOPAC coated nanoconjugates.

### **Modification of nanocomposite surface coating modulates subcellular localization of nanoconstructs**

Using Cryo-X-ray fluorescence microscopy (Cryo-XFM) we examined whether bare, DOPAC and MIBG coated nanoconstructs are transported to different subcellular locations after uptake. XFM provides complete elemental spectra for each pixel of the raster scanned sample and elemental distribution of biologically ubiquitous elements permits identification of cells and subcellular organelles. In figures of XFM maps, sulfur (S) outlines the area of the whole cells because S is a common element in all cellular proteins due to presence of methionine and cysteine amino acids.(Ortega et al. 2004 14719876) Zinc (Zn) is present throughout the cell as well, and it is especially abundant in the nucleus, (Finney et al. 2007 17283338; Glesne et al. 2006 16495082; Paunesku et al. 2003 12692534) while the presence of manganese (Mn) indicates locations of mitochondria primarily because of the concentrated presence of Manganese Superoxide Dismutase (MnSOD).(Paunesku et al. 2003 12692534; Paunesku et al. 2007 17274661) Iodine (I) background in cells is extremely low; this permitted us to use I as a proxy for MIBG distribution. 10 keV incident X-rays excited fluorescence of L shell electrons of I. Colocalization of characteristic K alpha electron shell signals of Ti and Fe indicates the position of the metal-oxide component of nanoconjugates -  $\text{Fe}_3\text{O}_4@\text{TiO}_2$  nanocomposites themselves. XFM allows quantitative,

tomographic, elemental mapping of whole, non-sectioned cells and therefore enables precise measurement and mapping of nanocomposite/nanoconjugate distribution in cells. Moreover, since X-ray fluorescence is an inherent elemental property this mode of imaging allows for detection of nanoconjugates/nanocomposites without necessitating the addition of dyes to the particle for detection, which could significantly alter the functional properties of that nanoparticle.(Grätzel 2004 ; Rajh et al. 2002) In recent years, use of Cryo-XFM has been implemented at the Advanced Photon Source (APS) at Argonne National Laboratory (ANL) with the Bionanoprobe instrument or with the use of the cryo-jet at the 2ID-D beamline. Images obtained with cryogenic technique show elemental content of the cells without elemental re-distribution that can be caused by fixation or drying. Using Cryo-XFM, we observed that bare nanocomposites (Fig. 2a) as indicated by Ti and Fe show a punctate cytoplasmic distribution pattern in SK-N-AS cells. Separation between the cell nucleus (area of the strongest Zn signal) and nanocomposite aggregates was confirmed by imaging of the sample rotated to 45 degrees (Fig. 2b). In Figs. 2c-d, we examined the pattern of distribution of DOPAC coated nanocomposites. Two distinct modes of distribution were observed for cells treated with DOPAC-nanoconjugates. The first, presented in Fig. 2c, was a large aggregation of nanocomposites while the second, in Fig. 2d, was a punctate distribution of smaller nanocomposite aggregates. Nevertheless, this cell too had a large aggregate associated with its perimeter. Cells treated with MIBG nanoconjugates showed only a punctate distribution pattern for Ti and Fe (Fig. 2e-g), with small puncta that were associated with I signal as well. Cells treated with nanoconjugates without MIBG only showed background I signal. Interestingly, several MIBG- $\text{Fe}_3\text{O}_4$ @ $\text{TiO}_2$  aggregates co-localized with Mn, a marker for mitochondria. Repeated scans of areas of interest containing nanoconjugate puncta were done after +/- 60-degree rotations. While elemental co-localization between Ti and Mn was still observed for several of the aggregates (Fig. 2f), aggregate nc1 was localized in the perinuclear region, rather than within the nucleus itself (Fig. 2g).

Previous reports showed that distribution of MIBG molecule is cytoplasmic and mitochondrial in neuroblastoma cells.(Gaze et al. 1991 2010230) The study that established this finding implemented electron spectroscopic imaging of thin sectioned cells. However, elemental sensitivity in this work was limited and some have even hypothesized that MIBG diffusion throughout the cell and subcellular compartments may be an artifact of fixation.(Clerc et al. 1993 8355077) In an effort to prevent MIBG redistribution and obtain information about cells that were not sectioned, we used cryo-XFM to image iodine distribution in MIBG treated whole frozen hydrated cells. Cryogenic conditions were found to preserve cellular architecture as well as the distribution of small molecules in cultured cells, unlike chemical fixation.(Chen et al. 2014 24365918)

SK-N-AS and SK-N-DZ cells were grown on silica nitride windows, treated with MIBG, frozen and imaged by Cryo-XFM (Supplemental Fig. 3a-c). Iodine was distributed through the cytoplasm and perinuclear areas, with very little iodine signal overlapping with the nucleus (Zn). Contrary to previous studies, we demonstrated that MIBG is not localized only to the mitochondria. This finding is confirmed by high resolution scans of the mitochondria in SK-N-AS (Supplemental Fig. 3c) and SK-N-DZ (Supplemental Fig. 3d) cells. Supplemental Fig. 3e presents a table of the average iodine concentration ratios in the

cytoplasm vs. nucleus and the mitochondria vs. cytoplasm. It is important to note that any of the iodine concentration can be associated with the is an artifact of whole cell imaging when tomographic mapping is not done. In such a case the iodine in the cytoplasmic layer directly above the nucleus is erroneously interpreted as nucleus associated signal when whole cell imaging is performed in 2D. Similar patterns of MIBG distribution were observed in cells treated with lower concentrations of this molecule (Supplemental Fig. 4).

Neither free MIBG nor MIBG coated nanoconjugates were observed in neuroblastoma cell nuclei as shown in Fig. 2 and Supplemental Fig. 3. In an effort to determine if MIBG-  $\text{Fe}_3\text{O}_4@\text{TiO}_2$  can reach the nucleus, we have added onto nanocomposite surface a targeting moiety an EGF mimicking “B-loop” peptide.(Yuan et al. 2013 24219664) We have previously shown that  $\text{Fe}_3\text{O}_4@\text{TiO}_2$  nanocomposites conjugated to this peptide bind to epidermal growth factor receptor (EGFR) and utilize the EGFR cellular trafficking to localize partially to the cell nucleus of HeLa cells.(Yuan et al. 2013 24219664) MIBG-  $\text{Fe}_3\text{O}_4@\text{TiO}_2$ -EGFB-loop-nanoconjugates were used to treat cells grown on silica nitride windows, at a concentration equivalent to 60  $\mu\text{M}$  MIBG and 637 nM nanocomposites. Treatment lasted for 90 minutes in serum free medium at 37 °C; windows were washed, plunge frozen in liquid ethane and imaged with the Bionanoprobe Xray fluorescence imaging instrument at APS. In Fig. 3a, elemental maps of an SK-N-AS cell treated with MIBG- $\text{Fe}_3\text{O}_4@\text{TiO}_2$ -B-loop nanoconjugates are presented. The nanoconjugates were detected within the nucleus, although the majority of nanoconjugates remaining in the cytoplasm. To confirm this finding, a full tomographic dataset of 2D maps covering a total rotation over 138 degrees was obtained. Image reconstruction and visualization at a variety of angles are shown in Fig. 3b-e and the Supplementary Video. Tomography confirmed nuclear localization of MIBG- $\text{Fe}_3\text{O}_4@\text{TiO}_2$ -B-loop nanoconjugates as indicated by the presence of Ti, Fe as well as I. Elemental quantification of Ti in a region of interest drawn for the nucleus accounted for 35.3% of complete Ti inside the cell, similar to our findings with nanocomposites coated with B-loop in the HeLa cell line.(Yuan et al. 2013 24219664) The trafficking of EGFR to the nucleus is partial (Dittmann et al. 2010 20692258; Dittmann et al. 2008 18789131; Lin et al. 2001 11533659; Lo et al. 2006 16552725; Wang et al. 2010 20674546; Wang et al. 2010 20937808) and only a portion of the targeted nanoconjugates can be expected to reach the nucleus. Figure 3f presents image of an SK-N-DZ cell from the cell sample treated with MIBG-  $\text{Fe}_3\text{O}_4@\text{TiO}_2$ -B-loop nanoconjugates at the same concentration as the SK-M-AS cell line. A full tomographic dataset for this cell was not obtained due to time constraints for tomographic XFM imaging; however, a strong overlap between the Zn signal (nucleus) and Ti signal (nanoconjugate) suggests that the nanoconjugate aggregate is spatially associated with the nucleus. Although it has been suggested that nuclear uptake can accommodate structures from 39 nm to 234 nm,(Misra and Sahoo 2010 19961929; Pante and Kann 2002 11854401; Paulo et al. 2011 22101232) larger aggregates that cannot completely translocate into the nucleus may nevertheless remain lodged in the nuclear membrane.

## Nanoconjugate surface coating influences cell viability in nanoconjugate treated neuroblastoma cells

We examined the effect of nanoconjugates on viability of neuroblastoma cell lines. Treatment with bare  $\text{Fe}_3\text{O}_4@\text{TiO}_2$  nanocomposites at concentrations up to 250 nM did not significantly affect viability of either SK-N-AS (Supplemental Fig. 5a), SK-N-DZ (Supplemental Fig. 5b) or NBL-W/S (Supplemental Fig. 5c) cell lines measured by MTS assay 72 hours after nanoconstructs treatment. However, viability of NBL-W/N cells (Supplemental Fig. 5d) treated with 250 nM bare nanocomposites was reduced to nearly 50%. MIBG molecule concentrations of up to 30  $\mu\text{M}$  had minimal effect on viability of SK-N-AS and SK-N-DZ cells (Supplemental Fig. 5e-f).

Interestingly, all four cell types have shown a statistically significant decrease in viability when treated with MIBG- $\text{Fe}_3\text{O}_4@\text{TiO}_2$  nanoconjugates (Fig. 4a-d). Maximal nanocomposite concentration tested was 250 nM while corresponding maximal concentration of MIBG was 23.59  $\mu\text{M}$ . Viability of SK-N-AS and NBL-W/S cells was affected only at the 250 nM concentration of MIBG- $\text{Fe}_3\text{O}_4@\text{TiO}_2$  nanoconjugates, while the loss of viability of SK-N-DZ cells was significant starting at 50 nM MIBG nanoconjugate concentration and at 100 nM concentration in cell line NBL-W/N. We also investigated if this effect on cell viability was notable only in neuroblastoma cells by investigating MIBG- $\text{Fe}_3\text{O}_4@\text{TiO}_2$  nanoconjugate effect on a non-neuroblastoma cell line, HeLa (Fig. 4e). These cells do not express a norepinephrine receptor critical for MIBG specific uptake.(Glowniak et al. 1993 8315492) We found that there was no significant difference in cytotoxicity between HeLa cells treated with bare nanocomposites or MIBG nanoconjugates. Finally, we examined if the effect of MIBG-nanoconjugates on cytotoxicity could be explained by a process whereby free MIBG could induce additional nanocomposite uptake or another cellular response, leading to the observed significant effect on cytotoxicity. When a co-treatment of SK-N-DZ cells was done with simultaneous addition of bare nanocomposites (100 nM) and free MIBG (in concentration of 9.3  $\mu\text{M}$ , equivalent to what was present on 100 nM MIBG coated nanoconjugates concentration) no significant decrease in viability was observed (Fig. 4f).

### **Decrease of cell viability caused by ionizing radiation is enhanced in the presence of DOPAC- $\text{Fe}_3\text{O}_4@\text{TiO}_2$ nanoconjugates**

Neuroblastoma cell lines used in this study differed significantly with respect to radiation sensitivity (Supplemental Fig. 6), with cell line SK-N-AS being the most radiation resistant. We evaluated the use of bare nanocomposites, free DOPAC and DOPAC coated  $\text{Fe}_3\text{O}_4@\text{TiO}_2$  nanoconjugates as possible radiation sensitizers (Fig. 5, Supplemental Fig. 7). Typically, a sensitizer enhancement ratio (SER) is calculated as the ratio of the dose necessary to achieve a particular level of cell killing in the absence of the sensitizer and in the presence of the sensitizer.(Tubiana 2005) In this case, we define the nanocomposite radiation enhancement ratio (NRER) to be the ratio of the percentage of cell viability at a particular radiation dose in the absence of nanocomposites to the percentage of viability in the presence of nanocomposites. An overview of cell viability is presented in Tables 1 and 2. Significant enhancement of radiation effects was observed in SK-N-AS cells for exposures to 2, 5, and 10 Gy in the presence of 250 nM bare nanocomposites. In SK-N-DZ cells, significant enhancement was observed at 5 and 10 Gy in the presence

of 250 nM bare nanocomposites. The calculated NRER for bare nanocomposites at 10 Gy was 1.2 for SK-N-AS cells and 1.24 for SK-N-DZ cells.

As detailed above, we noted conspicuous changes in uptake, subcellular localization, and size of aggregates of DOPAC- $\text{Fe}_3\text{O}_4$ @ $\text{TiO}_2$  nanoconjugates compared to bare nanocomposites. With respect to radiosensitization, these nanoconjugates showed different effects as well (Fig. 5c-d). In both SK-N-AS and SK-N-DZ cells, significant radiation sensitization was observed at 2, 5, and 10 Gy (Table 2) in combination with 100 and 250 nM nanoparticle concentrations. In this case, the NRER calculated for 250 nM DOPAC nanoconjugates at 10 Gy was 5.03 and 3.37 for SK-N-AS and SK-N-DZ cells, respectively. To examine if this effect could be due to DOPAC alone we repeated irradiations of neuroblastoma cells in the presence of DOPAC at molecular concentrations matching concentration of DOPAC bound to nanoparticles (Supplemental Fig. 7). Treatment of SK-N-AS and SK-N-DZ cells with concentrations of DOPAC equivalent to the DOPAC concentration bound to the nanocomposite surface (13  $\mu\text{M}$ , 33  $\mu\text{M}$ ), or even at significantly higher concentrations (50  $\mu\text{M}$ , 100  $\mu\text{M}$ ), had no additive or synergistic effect with irradiation in either cell line.

We then examined the mode of cell death in SK-N-AS cells, the most radio-resistant cell line in this study (Fig. 5e). SK-N-AS cells were exposed to 10 Gy of ionizing radiation alone, 250 nM DOPAC-nanoconjugates alone, or a combination of the two. Cells were then incubated for 24 hours, stained with Annexin-FITC and Propidium Iodide (PI), and evaluated by flow cytometry. Apoptosis was apparent in all treated samples. There was also a significant decrease in the number of live cells in samples treated with a combination of 10 Gy and DOPAC-nanoconjugates, compared to cells exposed either to 10 Gy alone or nanoconjugate alone. The percentage of live cells in 10 Gy and DOPAC-nanoconjugates treated cells was 70.43% at this time point, compared to 79.03% live cells after exposure to 10 Gy alone or 82.55% live cells after treatment with  $\text{DOPAC-Fe}_3\text{O}_4$ @ $\text{TiO}_2$  alone. There was also a significant increase in early apoptotic cells in samples exposed to 10 Gy and DOPAC-nanoconjugates (12.26%) compared to untreated control (3.7%).

DNA damage is the most important effect of irradiation and the primary cause of radiation induced cell death. To investigate the extent of double stranded DNA breaks in the presence of DOPAC- $\text{Fe}_3\text{O}_4$ @ $\text{TiO}_2$  nanoconjugates, we performed immunocytochemistry for p53 Binding Protein 1 (53BP1) foci (Fig. 5f, g). SK-N-AS cells were treated with 2 Gy radiation alone, 250 nM bare nanocomposites alone, 250 nM DOPAC- $\text{Fe}_3\text{O}_4$ @ $\text{TiO}_2$  nanoconjugates alone, or a combination of 2 Gy and either nanoconstruct. One hour after nanoconstruct treatment, cells were irradiated and allowed to recover in the incubator for 4 hours. Then the cells were fixed and stained for 53BP1 foci as indicators of double-stranded DNA breaks and the nuclei were counterstained with propidium iodide (PI). Foci were counted for at least 100 cells per treatment group and the percentage of cells with 20 or more foci was determined. At 0 Gy, as expected, the cells with 20 or more foci were few. At 2 Gy there was a notable increase in the number of foci in all samples, but the greatest increase was seen in irradiated cells pretreated with DOPAC-nanoconjugates. These results indicate that the cellular uptake of DOPAC-nanocomposites leads to an increased accumulation of DNA double strand breaks following irradiation with a dose as small as 2 Gy. It is worth

noting that this dose of gamma irradiation did not significantly decrease viability of either non-treated SK-N-AS cells nor pretreated cells with bare nanocomposites even with longer post irradiation incubation. (Table 1, Fig. 4a) However, the same experiments have shown that a 2 Gy exposure of cells previously treated with 250 nM DOPAC-nanoconjugates has led to a 47% decrease in cell viability (Table 2, Fig. 4c).

## Discussion

Neuroblastoma is a highly lethal pediatric cancer where nearly 50% of patients present with metastasis at the time of diagnosis.(DuBois et al. 1999 10363850; Maris et al. 2007 17586306) Recently, it has become evident that in patients who experience relapse, the recurrent tumor cells exhibit little resemblance to the original tumor genotype.(Eleveld et al. 2015 26121087; Schramm et al. 2015 26121086) New mutations in genes associated with RAS-MAPK pathway accumulate in the course of disease development contributing to a poor prognosis.(Eleveld et al. 2015 26121087; Schramm et al. 2015 26121086) Thus, many treatments that were initially successful become ineffective when relapse occurs.(Huang and Weiss 2013 24086065) Management of relapse requires aggressive therapies including radionuclide treatments that are often limited because of associated toxicities. Several recent clinical studies used either high dose or peptide modified MIBG based therapies. (Kayano et al. 2020 32219730; Sugiyama et al. 2020 32478419) Despite some promising findings of these studies, development of more efficient treatments that work on most neuroblastoma phenotypes and for refractory disease is critically important. Few recent studies using different nanotechnology platforms to target neuroblastomas suggest that bionanotechnology is a promising direction for research in neuroblastoma. (Alfei et al. 2020 32604768; Di Paolo et al. 2020 32323486)

In an effort to exploit nanotechnology to enhance currently available treatment modalities, this study has examined a core-shell  $\text{Fe}_3\text{O}_4@\text{TiO}_2$  nanocomposite as a potential radiosensitizer in neuroblastoma cell lines. The effects of bare, MIBG and DOPAC coated  $\text{Fe}_3\text{O}_4@\text{TiO}_2$  nanocomposites alone or combined with radiation were evaluated in four neuroblastoma cell lines with dissimilar genetic makeup. In general, the cell line SK-N-AS showed the greatest resistance to radiation and both bare and DOPAC coated  $\text{Fe}_3\text{O}_4@\text{TiO}_2$  nanoconjugates. In contrast, SK-N-DZ and NBL-W/N cell lines were sensitive to nanocomposites on their own as well as radiation alone. Combined use of radiation and nanocomposites led to more cell death than either treatment alone in SK-N-AS and SK-N-DZ cell lines. Interestingly, enhancement of radiation caused loss of cell viability caused by the presence of nanoconstructs was similar in both cell lines.

Exploiting the native cellular mechanisms of endocytosis and nuclear translocation of activated EGFR(Dittmann et al. 2010 20692258; Dittmann et al. 2008 18789131; Lin et al. 2001 11533659; Lo et al. 2006 16552725; Wang et al. 2010 20674546; Wang et al. 2010 20937808), we had previously used EGF mimicking peptide to promote cellular uptake and nuclear translocation of  $\text{Fe}_3\text{O}_4@\text{TiO}_2$  nanoconjugates. (Yuan et al. 2013 24219664) Neuroblastomas widely express EGFR,(Ho et al. 2005 16267010; Karmakar et al. 2009 19695221; Zage et al. 2013 22990745) and we used the same EGF mimicking peptide to

target nanoconstructs into nuclei of neuroblastoma cells as well.  $\text{Fe}_3\text{O}_4@\text{TiO}_2$  nanoconjugates without EGFR targeting peptide tend to accumulate in cytoplasm of SK-N-AS and SK-N-DZ neuroblastoma cells (Fig. 2). We anticipated this as we have found cytoplasmic distribution of other nontargeted nanoparticles in other types of cell lines in the past. (Arora et al. 2012 22158944; Brown et al. 2018 29541425; Thurn et al. 2011 20887814; Thurn et al. 2009 19242946) In contrast, XFM imaging has demonstrated that EGFR targeting peptide promoted cellular and nuclear localization of these nanoconjugates (Fig. 3). While EGFR targeting may deliver nanoconjugates to the cells, other peptides such as  $\text{G}_{\text{D}2}$  disialoganglioside could be used for targeting as well.  $\text{G}_{\text{D}2}$  disialoganglioside is expressed on 98% of neuroblastoma cells and it is already in use for antibody-based neuroblastoma therapies. (Iavarone et al. 1993 8417824; Maris et al. 2007 17586306)

MIBG has been shown to accumulate in nearly 85–90% of neuroblastoma through their expression of adrenaline/norepinephrine transporters.(Carlin et al. 2003 12960120) Radioactive  $^{131}\text{I}$  MIBG is currently used for diagnosis(Paltiel et al. 1994 8259387) as well as the treatment of high risk and refractory neuroblastoma.(Kayano et al. 2020 32219730; Matthay et al. 2007 17369569; Sugiyama et al. 2020 32478419)  $^{131}\text{I}$  is a long-range beta emitter with electrons traveling up to 2 mm and gamma emitter producing photons of 364 keV. Therefore  $^{131}\text{I}$  containing tumor cells and adjacent non-malignant cells are all affected by this treatment.(Cunningham et al. 1998 9649115) In this study, we confirmed previous assessment that MIBG may accumulate in mitochondria,(Gaze et al. 1991 2010230) as well as cytosol (Supplemental Figs. 3 and 4). MIBG coated nanoconjugates did appear associated with the same cellular regions as well (Fig. 2). Nevertheless, radiosensitization of cells treated with MIBG nanoconjugates was less than 1.5-fold and further studies will be necessary to explore possible advantages of MIBG coated nanoparticle preparation.

## Conclusions

Our studies demonstrated that administration of bare and MIBG coated  $\text{Fe}_3\text{O}_4@\text{TiO}_2$  nanocomposites led to a modest increase in radiation effects on several neuroblastoma cell lines exposed to external beam radiation. On the other hand, DOPAC coated nanocomposites despite aggregation and low cellular uptake dramatically increased sensitivity to radiation treatment in the neuroblastoma cells tested. Distribution of nanoconstructs and free MIBG in cells was studied by X-ray fluorescence microscopy. All non-targeted nanoconstructs accumulated, as expected in cytoplasm and, occasionally mitochondria. Nanocomposites targeted through the presence of the an EGF mimicking peptide, on the other hand, partially entered cell nuclei. An attractive potential future avenue of research would be to target radiolabeled MIBG molecules into the cell nucleus via the EGF mimicking peptide. Such nanoconjugates could act as radiosensitizers as well as deliver internal emitters close to genomic DNA.

## Methods:

### Nanocomposite Synthesis and Characterization:

$\text{Fe}_3\text{O}_4$  core and  $\text{TiO}_2$  shell NPs ( $\text{Fe}_3\text{O}_4@\text{TiO}_2$ ) were synthesized through a modified low temperature alkaline hydrolysis method as previously described.(Arora et al. 2012 22158944)  $\text{Fe}_3\text{O}_4$  nanoparticle cores were synthesized by stirring a solution of  $\text{FeCl}_2$  and  $\text{FeCl}_3$  in 24 mM citric acid for 3 hours at room temperature. The mixture was then allowed to gel in static air at 70°C for 24 hours, forming the  $\text{Fe}_3\text{O}_4$  core nanoparticles 1.5 to 3 nm in size. This solution was chilled and stirred vigorously with the gradual addition of chilled  $\text{TiCl}_4$  in HCl at 4°C, allowing for the Ti shell to form. Elemental concentration determination of nanocomposite suspension was performed by measuring titanium and iron concentrations by ICP-MS, at the Northwestern University Quantitative Bioelemental Imaging Center on an X series II ICP-MS (Thermo scientific, West Palm Beach, FL). The calculation used to determine the molarity of nanocomposites was previously described,(Arora et al. 2012 22158944) using Atomic Force Microscopy (AFM) sizing calculations and elemental concentrations determined by ICP-MS.

Following synthesis,  $\text{Fe}_3\text{O}_4@\text{TiO}_2$  nanocomposites were dialyzed (dialysis tubing pore size = 2,000 MWCO) in 10 mM  $\text{Na}_2\text{HPO}_4$  (pH 4.5) and stored at 4°C. Under these conditions phosphate molecules attach to the nanoparticle surface; this preparation constituted “bare” nanocomposites. (Michelmore et al. 2000 WOS:000088087000021)

MIBG (Sigma-Aldrich, St. Louis, MO) was bound with 3,4-dihydroxyphenylacetic acid (DOPAC) through a peptide bond forming reaction using EDC (Thermo Scientific), following the manufacturer's instructions. The final concentration of MIBG-DOPAC was 2.34 mM. DOPAC was used as a linker because it has a high affinity for the surface of nano-sized  $\text{TiO}_2$  being a catechol. DOPAC also has a carboxyl group that can form a peptide bond with the amino group of MIBG.(Creutz and Chou 2008 18366179; Paunesku et al. 2007 17274661; Thurn et al. 2009 19242946)  $\text{Fe}_3\text{O}_4@\text{TiO}_2$  nanocomposites were mixed overnight with DOPAC-MIBG in an oxygen free atmosphere; the resultant nanoconjugates were dialyzed in 10 mM sodium phosphate buffer (dialysis pore size of 2,000 MWCO). Using a calculation approach previously described(Arora et al. 2012 22158944) we estimated that mixing DOPAC-MIBG solution as prepared V:V with 22.3  $\mu\text{M}$   $\text{Fe}_3\text{O}_4@\text{TiO}_2$  nanocomposites lead to DOPAC-MIBG covering roughly 70% of the nanoparticle surface.

DOPAC- $\text{Fe}_3\text{O}_4@\text{TiO}_2$  nanoconjugates were prepared by combining equal volumes of 7.838 mM DOPAC with 28.93  $\mu\text{M}$   $\text{Fe}_3\text{O}_4@\text{TiO}_2$  nanocomposites in an oxygen-free environment followed by mixing the conjugation reaction overnight at 4°C. DOPAC- $\text{Fe}_3\text{O}_4@\text{TiO}_2$  nanocomposites were then dialyzed for 2 hours in 10 mM  $\text{Na}_2\text{HPO}_4$  buffer. We estimated that under these circumstances molecules of DOPAC covered roughly 100% of the nanoparticle surface.

Elemental makeup and the shape of  $\text{Fe}_3\text{O}_4@\text{TiO}_2$ -MIBG nanoconjugates were evaluated by EDS-STEM which was performed at Northwestern University's Atomic and Nanoscale Characterization Experimental Center (Supplemental Figure 1a-c). In preparation for EDS-STEM,  $\text{Fe}_3\text{O}_4@\text{TiO}_2$ -MIBG nanoconjugates were diluted 1:100 in ddH<sub>2</sub>O, drop cast onto 150 square mesh copper grids with a carbon film support, allowed to dry, and then imaged on a Hitachi HD-2300 Dual EDS Cryo STEM (Supplemental Figure 1a).

Infrared determination of nanocomposite coating (Supplemental Figure 2) was performed using infrared spectroscopy at the Infrared Environmental Imaging (IRENI) instrument at University of Wisconsin Synchrotron Center. Droplets of different nanoconjugate colloids or component solutions were cast and dried on Ultralene membrane supports and scanned in 2D. Chemograms for the areas of interest were obtained. Addition of each new nanoconjugate coating can be followed by appearance of new spectral features (Supplemental Figure 2).

Zeta potential measurements of nanoconjugates were also obtained (Supplemental Table 1) using a protocol that was adapted from the procedure recommended by the Nanotechnology Characterization Laboratory at the National Cancer Institute.(Clogston 2009) Bare nanocomposites, DOPAC- $\text{Fe}_3\text{O}_4$ @ $\text{TiO}_2$ , and MIBG- $\text{Fe}_3\text{O}_4$ @ $\text{TiO}_2$  nanoconjugates were diluted 1:100 in 10 mM filtered NaCl using the following constants (temp: 25°C, viscosity: 0.891, dielectric constant: 78.6, Henry function: 1.5, refractive index: 1.33) on a Zeta sizer Nano (Malvern, Worcestershire, United Kingdom).  $\text{Fe}_3\text{O}_4$ @ $\text{TiO}_2$ -MIBG nanoconjugates have a mean ZP of  $-40.887 \pm 1.85$ , bare (phosphate covered)  $\text{Fe}_3\text{O}_4$ @ $\text{TiO}_2$  nanoconjugates have a mean ZP of  $-37.1 \pm 1.91$ , and DOPAC coated nanocomposites have a mean ZP of  $-33.367 \pm 0.71$ .

Nanosight measurements were also performed using a Nanosight LM10-HS (Malvern, Worcestershire, United Kingdom) in lieu of dynamic light scattering (Supplemental Table 2). Because of the polydispersity of nanocomposites, presence of nanocomposite aggregates and the non-spherical shape of these objects, these results are not as reliable a source of nanoparticle size information as the AFM or TEM data.

To further confirm the spatial and aggregation characteristics of different nanocomposites, Cryo-TEM (Figure 1a-c) was performed at the Northwestern University Biological Imaging Facility. Nanocomposite 1:100 dilutions in full media (DMEM + 10% FBS) of bare (phosphate coated)  $\text{Fe}_3\text{O}_4$ @ $\text{TiO}_2$  nanocomposites, DOPAC- $\text{Fe}_3\text{O}_4$ @ $\text{TiO}_2$  nanoconjugates, and MIBG- $\text{Fe}_3\text{O}_4$ @ $\text{TiO}_2$  nanoconjugates were drop cast on plasma treated lacy carbon TEM grids, plunge frozen in liquid ethane using a FEI Vitrobot Mark IV, and Cryo-TEM was performed using a JEOL 1230 TEM at 120 kV. Image brightness levels were adjusted to enhance contrast. The spatial and aggregation properties of different nanocomposites are similar, close to value obtained by AFM and smaller than the size estimates obtained from the light scattering measurements done with the Nanosight instrument.

EGFR B-loop peptide (DOPAC-MYIEALDKYAC-COOH) and scrambled peptide (DOPAC-EAKLDYMCYI-COOH) were synthesized by the IBNAM (now The Simpson Querrey Institute for Bionanotechnology) Core Facility of Northwestern University's Institute for Bionanotechnology in Medicine. The DOPAC group at the N-terminus of the peptide served as a linker to conjugate the peptide to the  $\text{TiO}_2$  surface of the nanoparticles. B-loop peptide was dissolved to a concentration of 700  $\mu\text{M}$  in ddH<sub>2</sub>O bubbled with N<sub>2</sub>, then mixed V:V with 22.3  $\mu\text{M}$  MIBG-nanocomposites or 28.93  $\mu\text{M}$  bare nanocomposites. A separate set of nanocomposites was conjugated to a scrambled peptide. The conjugation was performed in an oxygen

free atmosphere overnight at 4°C. At a concentration of 350 µM peptide and 11.15 µM MIBG-Fe<sub>3</sub>O<sub>4</sub>@TiO<sub>2</sub>, it was estimated that the B-loop peptide should cover roughly 23% of the MIBG-nanoparticle surface, while with bare nanocomposites the surface coverage was estimated to be roughly 18% (Arora et al. 2012 22158944). Experiments with cells in culture were performed within 4 hours following conjugation.

## Cell culture

Neuroblastoma cell lines SK-N-AS and SK-N-DZ and cervical cancer cell line HeLa were purchased from American Type Culture Collection (ATCC, Manassas, Virginia). These cells were grown in DMEM supplemented with 10% non-heat inactivated FBS with penicillin/streptomycin and non-essential amino acids at 37°C and 5% CO<sub>2</sub>. Neuroblastoma cell lines NBL-W/S and NBL-W/N were a generous gift from S.L. Cohn (Department of Pediatrics, University of Chicago, Chicago, IL). These cells were grown in RPMI-1640 medium supplemented with 10% heat inactivated FBS with penicillin/streptomycin and L-glutamine.

## Cell viability assay

SK-N-AS, SK-N-DZ, NBL-W/S, NBL-W/N, and HeLa cells were trypsinized, collected, counted, and plated (5-6 x 10<sup>3</sup> SK-N-AS cells per well, 6-7 x 10<sup>3</sup> SK-N-DZ, 9 x 10<sup>2</sup> NBL-W/S, 8-9 x 10<sup>3</sup> NBL-W/N, or 2.5 x 10<sup>3</sup> HeLa) into 96-well plates and allowed to attach overnight. Five to six wells for each cell line were used as biological replicates in each experiment. Cells were treated with varying concentrations of bare Fe<sub>3</sub>O<sub>4</sub>@TiO<sub>2</sub> nanocomposites, DOPAC-Fe<sub>3</sub>O<sub>4</sub>@TiO<sub>2</sub> nanoconjugates, MIBG-Fe<sub>3</sub>O<sub>4</sub>@TiO<sub>2</sub> nanoconjugates, free DOPAC, free MIBG, DMSO (control for free MIBG experiments), or Na<sub>2</sub>HPO<sub>4</sub> buffer (10 mM, vehicle control for nanocomposites). In radiosensitization experiments, cells were treated with nanocomposites or nanoconjugates for 1 hour, followed by varying doses of ionizing radiation. Cesium source (662 keV Gamma Irradiator (Gammacell 40, Atomic Energy of Canada Ltd.) was used under the supervision of the Office of Research Safety, Health Physics Services, Northwestern University.

Nanocomposite/nanoconjugate and irradiation treatments were performed in complete media over a period of 72 hours. Equivalent “blank” wells without cells, but with an identical concentration of treatment reagents were used as blank controls (n=5), in order to account for any possible modification of absorbance readout that could occur because of the treatment materials used. After incubation, a tetrazolium compound [3-(4,5-dimethylthiazol-2-yl)-5-(3-carboxymethoxyphenyl)-2-(4-sulfophenyl)-2H-tetrazolium, inner salt] (MTS reagent, Promega, Madison WI) was added as 1/10<sup>th</sup> of the volume into each well, and the 96 well plates were incubated an additional 2-4 hours at 37°C. Initially, treatment media was removed from both treatment and blank wells before adding MTS and new media; this approach was discontinued when no significant differences in results were observed when MTS was added to wells without any prior manipulation. The latter approach was used subsequently in order to mitigate the risk of inadvertent removal of less adherent cells. Absorbance readings were measured using a SpectraMax M5 (Molecular Devices, Sunnyvale, CA) plate reader at 490 nm. Absorbance values measured for “blank” controls were averaged and subtracted from the treatment values. Resultant absorbance value was

divided by the average of the absorbance values for each respective negative control, providing percentage of cell viability as a function of the control (surviving fraction). For radiation sensitization determination, each adjusted absorbance value was divided by the average of each treatment group respective baseline (cells treated with nanocomposites or nanoconjugates but not exposed to radiation) absorbance, to obtain an adjusted percentage of survival, to account for baseline cell death.

### Evaluation of nanocomposite and nanoconjugate uptake by ICP-MS

SK-N-AS and SK-N-DZ cells were trypsinized, counted, and plated ( $5\text{-}8 \times 10^5$  of SK-N-AS cells, or  $6\text{-}10 \times 10^5$  SK-N-DZ cells) onto 6-well plates and allowed to attach overnight. Empty wells with identical treatment conditions were also prepared, to act as a control for potential artifacts such as adherence of nanocomposites to the bottom of the wells in absence of cells. Additional wells seeded with an identical number of SK-N-AS or SK-N-DZ cells were used to estimate the final number of cells per well at the conclusion of experiment and to determine background elemental concentrations. Treatments with 250 nM bare  $\text{Fe}_3\text{O}_4@\text{TiO}_2$  nanocomposites, 250 nM DOPAC- $\text{Fe}_3\text{O}_4@\text{TiO}_2$  nanocomposites, or 250nM MIBG- $\text{Fe}_3\text{O}_4@\text{TiO}_2$  nanoconjugates were done in compete media (total volume of media per well was 1 ml) for 1 hour at 37°C; three wells per treatment represented biological replicates. After treatment, the wells were washed 1-3 times with PBS and once with acidic glycine. Finally, 500  $\mu\text{L}$  of 70%  $\text{HNO}_3$  (re-distilled, >99.999% trace metal basis) was added per well and cells and nanoconjugates were digested for 2 hours at room temperature. Samples were then transferred into 15ml metal-free Falcon tubes, mixed with 10 mL 3%  $\text{HNO}_3$  in ddH<sub>2</sub>O containing 3 ppb  $^{115}\text{In}$  (as an internal control), and allowed to digest additionally overnight at 70°C. Samples were evaluated for elemental concentrations of  $^{47}\text{Ti}$ ,  $^{57}\text{Fe}$ , and  $^{115}\text{In}$  using an X series II ICP-MS. Ti concentration was used as a proxy for nanoparticle/nanoconjugate concentration. Average background elemental quantity obtained from cell free nanocomposite treated blank wells was subtracted from each test sample, to arrive at a final total concentration of nanocomposites taken up by cells. This number was divided by the “end of experiment” cell count to arrive at a Ti concentration per  $10^5$  cells. Uptake of bare nanocomposites was used as a standard and uptake of nanoconjugates was expressed as a percentage of the Ti concentration found for uncoated nanocomposites.

### Evaluation of Apoptosis/Necrosis by Flow Cytometry

SK-N-AS cells were seeded onto 6-well plates ( $2 \times 10^5$  cells per well) and allowed to attach overnight. Cells treated with 250 nM DOPAC- $\text{Fe}_3\text{O}_4@\text{TiO}_2$  nanocomposites for one hour as well as untreated controls were either sham irradiated or exposed to 10 Gy of gamma rays from a  $^{137}\text{Cs}$  irradiator. Cells were then incubated for 24 hours, washed with PBS, trypsinized and processed according to manufacturer’s instructions.  $10^5$  cells in 100  $\mu\text{L}$  of annexin binding buffer were incubated with Annexin-FITC and Propidium Iodide (PI) for 15 minutes at room temperature, placed on ice, and immediately evaluated by flow cytometry using a BD LSR Fortessa Analyzer (BD Biosciences, Franklin Lakes, NJ) at the Robert H. Lurie Comprehensive Cancer Center Flow Cytometry Core Facility at Northwestern University. For each biological replicate, 5000 gated events were analyzed.

## Evaluation of 53BP1 Foci

A total of 200,000 SK-N-AS cells were seeded onto barrier slides and allowed to attach overnight. Cells in 1 ml full medium were then treated with varying concentrations of DOPAC- $\text{Fe}_3\text{O}_4@\text{TiO}_2$  nanoconjugates or bare nanocomposites for 1 hour. Cells were then irradiated with 2 Gy and incubated for 4 hours. Slides were washed with PBS and cells fixed in 3.6% formaldehyde for 10 minutes at room temperature. Cells were then permeabilized with PBS-Triton (0.2%) for 10 min, rinsed three times with PBS-BSA (1%) – Tween (0.5%) and processed further in the same buffer. Slides were incubated for 1h with primary antibody against 53BP1 (ab21083 – Abcam, Cambridge, UK) used at 1:200 dilution, washed and incubated for 45 minutes with fluorescent secondary antibody (Alexa Fluor 488 – Goat Anti-Rabbit, ab150077, Abcam, Cambridge UK). Nuclei were counterstained with propidium iodide (2.5  $\mu\text{g}/\text{ml}$ ). Cells were imaged at 40x magnification with a full field fluorescent Zeiss microscope equipped with a CoolSNAP EZ CCD camera (Photometrics, Tucson AZ, US).

Four experiments were performed with two replicate slides for each treatment condition conducted. The 53BP3 foci in each replicate were counted by a different researcher. Multiple images of each slide were taken, and foci present in at least 100 cells were counted for each treatment group. All experiments were pooled as indicated (slide numbers ranged between 3 and 7) and statistics generated from the pooled data.

## Cryogenic X-ray fluorescence microscopy (Cryo-XFM)

SK-N-AS and SK-N-DZ cells were seeded on 1.5 mm x 1.5 mm  $\text{Si}_3\text{N}_4$  windows overnight (Silson, UK), then treated either with 4.24  $\mu\text{M}$  MIBG (with a resultant 0.05% DMSO concentration), 25.44  $\mu\text{M}$  MIBG (final 0.30% DMSO), 60  $\mu\text{M}$  MIBG (final 2% DMSO), or DMSO control (0.30% DMSO) in 50  $\mu\text{L}$  of full media for 90 minutes. In nanocomposite treatment experiments, cells were treated with MIBG- $\text{Fe}_3\text{O}_4@\text{TiO}_2$ -B-Loop nanoconjugates (carrying an equivalent of 60  $\mu\text{M}$  of MIBG) for 90 minutes in serum-free DMEM. In addition, another set of cells grown on  $\text{Si}_3\text{N}_4$  windows were exposed to 250 nM MIBG- $\text{Fe}_3\text{O}_4@\text{TiO}_2$ , 250 nM DOPAC- $\text{Fe}_3\text{O}_4@\text{TiO}_2$ , or 250nM of bare (phosphate covered)  $\text{Fe}_3\text{O}_4@\text{TiO}_2$  nanocomposites for 60 minutes in 50  $\mu\text{L}$  of full media. The windows were washed twice in a Tris glucose buffer (261 mM glucose, 9 mM acetic acid, 10 mM Tris buffer, pH 7.4) and plunge frozen in liquid ethane using a FEI Vitrobot Mark IV. Frozen hydrated cells were imaged with visible light on a Nikon microscope equipped with an Instec CLM77KCryo-LM stage in order to evaluate the quality of each sample with regard to ice accumulation as well as cell density and distribution.

X-ray fluorescence imaging was done with several different instruments under different conditions. A beam spot size of about 300 or 600 nm was used at the sector 2-ID-D at APS at ANL in combination with a cryo-jet; while the Bionanoprobe at sector 21 LS-CAT was used with a beam spot size 85 nm, and the samples were maintained in vacuum at liquid nitrogen temperature. High-resolution elemental maps were obtained at different angles, allowing subsequent tomographic reconstruction. A monochromatic 10 keV X-ray beam was used and the cells were scanned in “continuous” (fly-scan) mode. Step scans for an area

of interest were also done at a step size of 80 nm and per pixel dwell time of 3 sec. To minimize background noise, a Gaussian smoothing filter ( $\sigma = 2/3$ ) was applied to the images in the figures presented.

For tomographic reconstruction, scans were done at multiple angles (3-degree increments, total angular range of 138 degrees); reconstructions were performed in Mathematica 9.0 (Wolfram Research, Champaign, IL). In order to circumvent misalignment of particles as a result of sample movement during scanning, the “displacement” of particles with clear projections (Cl, I, K, P and S) was analyzed, and the average shift along the x and y axis of these particles was calculated. Correction of any displacement of the tested particles was achieved by applying this calculated shift to all the particles, hence any misalignment was adjusted. Tomographic reconstruction was attained by implementing a modified Simultaneous Iterative Reconstruction Technique (SIRT) rather than Filtered Back Projection (FBP) since the later yields poor images owing to the limited number of projections. Use of SIRT was described previously with the final visualization of elemental signals of interest using Avizo (FEI, Burlington, MA). (Vo et al. 2014 25320994) Elemental concentration data were extracted for each pixel of the 2D images (elemental quantification, per-pixel fitting) using the MAPS program.(Vogt et al. 2003)

## Statistical analyses

All comparisons were performed using student’s T-test at a significance level of 0.05. Data points in all figures correspond to mean +/- standard deviation.

## Abbreviations

53BP1 p53 Binding Protein 1

AFM Atomic Force Microscopy

APS Advanced Photon Source

ANL Argonne National Laboratory

DNA Deoxyribonucleic Acid

DOPAC 3,4-Dihydroxyphenylacetic acid

EDS Energy-dispersive X-ray spectroscopy

EDC 1-ethyl-3-(3-dimethylaminopropyl) carbodiimide hydrochloride

EGF Epidermal Growth Factor

EGFR Epidermal Growth Factor Receptor

$\text{Fe}_3\text{O}_4$  Iron oxide

$\text{Fe}_3\text{O}_4 @ \text{TiO}_2$  Iron oxide core, Titanium dioxide shell nanocomposite

ICP-MS Inductively coupled plasma mass spectrometry

IRENI Infrared Environmental Imaging

MIBG Metaiodobenzylguanidine

MTS 3-(4,5-dimethylthiazol-2-yl)-5-(3-carboxymethoxyphenyl)-2-(4-sulfophenyl)-2H-tetrazolium

MYCN N-myc proto-oncogene protein

NRER Nanocomposite radiation enhancement ratio

TEM Transmission Electron Microscope

$\text{TiO}_2$  Titanium dioxide

S-type Epithelial morphology in neuroblastoma

SER Sensitizer enhancement ratio

STEM Scanning Transmission Electron Microscope

RAS-MAPK RAS-Mitogen-activated protein kinase

ROI Region of Interest

XFM X-ray fluorescence microscopy

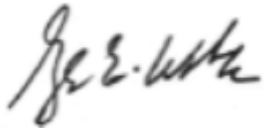
## Declarations

## Ethics approval and consent to participate

Not applicable.

## Consent for publication

I, the corresponding author, Gayle E Woloschak give consent for publication of this manuscript on behalf of all authors.



## Availability of data and materials

All data generated or analyzed during this study are included in this published article and its supplementary information files.

### Competing interests

Authors have no competing interests to declare

## Funding

This work was supported by the NIH grants CA107467, EB002100, GM104530 and U54 CA151880 and U54CA119341 and a generous gift from Make Your Mark Foundation (<http://makeyourmark7.org/>). WL was supported in part by the Northwestern University Biotechnology Biotechnology Cluster Training Grant. XFM was performed at the Advanced Photon Source at Argonne National Laboratory at XOR beamlines 2-ID-D, 2-ID-E, and LS-CAT 21-ID-D Bionanoprobe; this instrument was obtained through an NIH ARRA S10 grant SP0007167. Work at Argonne National Laboratory was supported by the U.S. Department of Energy, Office of Science, Office of Basic Energy Sciences, Contract No. DE-AC02-06CH11357. We also thank Argonne National Laboratory for support under LDRD project 2013-168-N0.

## Authors' contributions

William Liu and Salida Mirzoeva conceived and conducted experiments and conducted data analysis; Ye Yuan, Junjing Deng, Si Chen, Barry Lai Karna Shah, Rahul Shroff, Julia Sedlmair and Qiaoling Jin conducted experiments, Reiner Bleher contributed to experimental design; Nghia Vo conducted data analysis, Remon Bazak, Carissa Ritner, Stanley Gutionov and Sumita Raha participated in manuscript preparation, Stefan Vogt and Carol Hirschmugl contributed to data analysis, Tatjana Paunesku contributed to project design, conducted experiments and contributed to manuscript preparation, Chris Jacobsen and John Kalapurkal contributed to project conception, and Gayle E. Woloschak contributed to project conception, design and manuscript preparation

## Acknowledgements

Cryo EDS-STEM was performed by Charlene Wilke at Northwestern University's Atomic and Nanoscale Characterization Experimental Center (NUANCE). ICP-MS was performed with help from Keith MacRenaris

at Northwestern University's Quantitative Bioelemental Imaging Center (QBIC).

## References

1. Alfei S, Marengo B, Zuccari G, Turrini F, Domenicotti C. (2020) Dendrimer Nanodevices and Gallic Acid as Novel Strategies to Fight Chemoresistance in Neuroblastoma Cells Nanomaterials (Basel, Switzerland) 10 doi:10.3390/nano10061243.
2. Arora HC, Jensen MP, Yuan Y, Wu A, Vogt S, Paunesku T, Woloschak GE. Nanocarriers enhance Doxorubicin uptake in drug-resistant ovarian cancer cells. *Cancer Res.* 2012;72:769–78. doi:10.1158/0008-5472.CAN-11-2890.
3. Aygun N. Biological and Genetic Features of Neuroblastoma and Their Clinical Importance. *Curr Pediatr Rev.* 2018;14:73–90. doi:10.2174/1573396314666180129101627.
4. Baade PD, Youlden DR, Valery PC, Hassall T, Ward L, Green AC, Aitken JF. Trends in incidence of childhood cancer in Australia, 1983–2006. *Br J Cancer.* 2010;102:620–6. doi:10.1038/sj.bjc.6605503.
5. Bazak R, Houri M, Achy SE, Hussein W, Refaat T. Passive targeting of nanoparticles to cancer: A comprehensive review of the literature. *Mol Clin Oncol.* 2014;2:904–8. doi:10.3892/mco.2014.356.
6. Bazak R, Houri M, El Achy S, Kamel S, Refaat T. Cancer active targeting by nanoparticles: a comprehensive review of literature. *J Cancer Res Clin Oncol.* 2015;141:769–84. doi:10.1007/s00432-014-1767-3.
7. Bazak R, et al. Cytotoxicity and DNA cleavage with core-shell nanocomposites functionalized by a KH domain DNA binding peptide. *Nanoscale.* 2013;5:11394–9. doi:10.1039/c3nr02203j.
8. Blake DM, Maness P-C, Huang Z, Wolfrum EJ, Huang J, Jacoby WA. Application of the Photocatalytic Chemistry of Titanium Dioxide to Disinfection and the Killing of Cancer Cells Separation. and Purification Methods. 1999;28:1–50. doi:10.1080/03602549909351643.
9. Brown K, et al. Intracellular in situ labeling of TiO(2) nanoparticles for fluorescence microscopy detection. *Nano Res.* 2018;11:464–76. doi:10.1007/s12274-017-1654-8.
10. Carlin S, et al. Development of a real-time polymerase chain reaction assay for prediction of the uptake of meta-[<sup>131</sup>I]iodobenzylguanidine by neuroblastoma tumors. *Clin Cancer Res.* 2003;9:3338–44.
11. Chagnovich D, Cohn SL. Activity of a 40 kDa RNA-binding protein correlates with MYCN and c-fos mRNA stability in human neuroblastoma. *Eur J Cancer.* 1997;33:2064–7. doi:10.1016/s0959-8049(97)00208-6.
12. Chen S, et al. The Bionanoprobe: hard X-ray fluorescence nanoprobe with cryogenic capabilities. *J Synchrotron Radiat.* 2014;21:66–75. doi:10.1107/S1600577513029676.
13. Clerc J, Halpern S, Fourre C, Omri F, Briancon C, Jeusset J, Fragu P. SIMS microscopy imaging of the intratumor biodistribution of metaiodobenzylguanidine in the human SK-N-SH neuroblastoma cell line xenografted into nude mice. *J Nucl Med.* 1993;34:1565–70.

14. Clogston JD. (2009) NCL Method PCC-2 Measuring Zeta Potential of Nanoparticles..  
[http://ncl.cancer.gov/NCL\\_Method\\_PCC-2.pdf](http://ncl.cancer.gov/NCL_Method_PCC-2.pdf). 2020.
15. Cooke MS, Evans MD, Dizdaroglu M, Lunec J. Oxidative DNA damage: mechanisms, mutation, and disease. *FASEB J.* 2003;17:1195–214. doi:10.1096/fj.02-0752rev.
16. Creutz C, Chou MH. Binding of catechols to mononuclear titanium(IV) and to 1- and 5-nm TiO<sub>2</sub> nanoparticles. *Inorg Chem.* 2008;47:3509–14. doi:10.1021/ic701687k.
17. Cunningham SH, Mairs RJ, Wheldon TE, Welsh PC, Vaidyanathan G, Zalutsky MR. Toxicity to neuroblastoma cells and spheroids of benzylguanidine conjugated to radionuclides with short-range emissions. *Br J Cancer.* 1998;77:2061–8. doi:10.1038/bjc.1998.348.
18. Di Paolo D, et al. Combined Replenishment of miR-34a and let-7b by Targeted Nanoparticles Inhibits Tumor Growth in Neuroblastoma. *Preclinical Models Small.* 2020;16:e1906426.  
doi:10.1002/smll.201906426.
19. Dittmann K, Mayer C, Fehrenbacher B, Schaller M, Kehlbach R, Rodemann HP. Nuclear EGFR shuttling induced by ionizing radiation is regulated by phosphorylation at residue Thr654. *FEBS Lett.* 2010;584:3878–84. doi:10.1016/j.febslet.2010.08.005.
20. Dittmann K, Mayer C, Kehlbach R, Rodemann HP. Radiation-induced caveolin-1 associated EGFR internalization is linked with nuclear EGFR transport and activation of. *DNA-PK Mol Cancer.* 2008;7:69. doi:10.1186/1476-4598-7-69.
21. DuBois SG, et al. Metastatic sites in stage IV and IVS neuroblastoma correlate with age, tumor biology, and survival. *J Pediatr Hematol Oncol.* 1999;21:181–9. doi:10.1097/00043426-199905000-00005.
22. DuBois SG, Matthay KK. Radiolabeled metaiodobenzylguanidine for the treatment of neuroblastoma. *Nucl Med Biol.* 2008;35(Suppl 1):35–48. doi:10.1016/j.nucmedbio.2008.05.002.
23. Eleveld TF, et al. Relapsed neuroblastomas show frequent RAS-MAPK pathway mutations. *Nat Genet.* 2015;47:864–71. doi:10.1038/ng.3333.
24. Finney L, et al. X-ray fluorescence microscopy reveals large-scale relocalization and extracellular translocation of cellular copper during angiogenesis. *Proc Natl Acad Sci U S A.* 2007;104:2247–52.  
doi:10.1073/pnas.0607238104.
25. Foley J, Cohn SL, Salwen HR, Chagnovich D, Cowan J, Mason KL, Parysek LM. Differential expression of N-myc in phenotypically distinct subclones of a human neuroblastoma cell line. *Cancer Res.* 1991;51:6338–45.
26. Gatta G, et al. Embryonal cancers in Europe. *Eur J Cancer.* 2012;48:1425–33.  
doi:10.1016/j.ejca.2011.12.027.
27. Gaze MN, Huxham IM, Mairs RJ, Barrett A. Intracellular localization of metaiodobenzyl guanidine in human neuroblastoma cells by electron spectroscopic imaging. *Int J Cancer.* 1991;47:875–80.  
doi:10.1002/ijc.2910470615.
28. Glesne D, Vogt S, Maser J, Legnini D, Huberman E. Regulatory properties and cellular redistribution of zinc during macrophage differentiation of human leukemia cells. *J Struct Biol.* 2006;155:2–11.

- doi:10.1016/j.jsb.2005.09.012.
29. Glowniak JV, Kilty JE, Amara SG, Hoffman BJ, Turner FE. Evaluation of metaiodobenzylguanidine uptake by the norepinephrine, dopamine and serotonin transporters. *J Nucl Med*. 1993;34:1140–6.
30. Grätzel M. Conversion of sunlight to electric power by nanocrystalline dye-sensitized solar cells. *Journal of Photochemistry Photobiology A Chemistry*. 2004;164:3–14.  
doi:10.1016/j.jphotochem.2004.02.023.
31. Ho R, et al. Proliferation of human neuroblastomas mediated by the epidermal growth factor receptor. *Cancer Res*. 2005;65:9868–75. doi:10.1158/0008-5472.CAN-04-2426.
32. Huang M, Weiss WA. Neuroblastoma and MYCN *Cold Spring. Harb Perspect Med*. 2013;3:a014415.  
doi:10.1101/cshperspect.a014415.
33. Iavarone A, Lasorella A, Servidei T, Riccardi R, Mastrangelo R. Uptake and storage of m-iodobenzylguanidine are frequent neuronal functions of human neuroblastoma cell lines. *Cancer Res*. 1993;53:304–9.
34. Kacar A, et al. Solid tumors in Turkish children: a multicenter study. *World J Pediatr*. 2013;9:25–31.  
doi:10.1007/s12519-011-0323-3.
35. Karmakar S, Davis KA, Choudhury SR, Deeconda A, Banik NL, Ray SK. Bcl-2 inhibitor and apigenin worked synergistically in human malignant neuroblastoma cell lines and increased apoptosis with activation of extrinsic and intrinsic pathways *Biochem. Biophys Res Commun*. 2009;388:705–10.  
doi:10.1016/j.bbrc.2009.08.071.
36. Kayano D, et al. High-dose (<sup>131</sup>I)-metaiodobenzylguanidine therapy in patients with high-risk neuroblastoma in Japan *Annals. of nuclear medicine*. 2020;34:397–406. doi:10.1007/s12149-020-01460-z.
37. Kim B, van Golen CM, Feldman EL. Insulin-like growth factor-I signaling in human neuroblastoma. *cells Oncogene*. 2004;23:130–41. doi:10.1038/sj.onc.1206924.
38. Lin SY, et al. Nuclear localization of EGF receptor and its potential new role as a transcription factor. *Nat Cell Biol*. 2001;3:802–8. doi:10.1038/ncb0901-802.
39. Lo HW, Ali-Seyed M, Wu Y, Bartholomeusz G, Hsu SC, Hung MC. Nuclear-cytoplasmic transport of EGFR involves receptor endocytosis, importin beta1 and CRM1. *J Cell Biochem*. 2006;98:1570–83.  
doi:10.1002/jcb.20876.
40. Maris JM. Recent advances in neuroblastoma *N. Engl J Med*. 2010;362:2202–11.  
doi:10.1056/NEJMra0804577.
41. Maris JM, Hogarty MD, Bagatell R, Cohn SL. Neuroblastoma *Lancet*. 2007;369:2106–20.  
doi:10.1016/S0140-6736(07)60983-0.
42. Matthay KK, George RE, Yu AL. Promising therapeutic targets in neuroblastoma. *Clin Cancer Res*. 2012;18:2740–53. doi:10.1158/1078-0432.CCR-11-1939.
43. Matthay KK, et al. Phase II study on the effect of disease sites, age, and prior therapy on response to iodine-131-metaiodobenzylguanidine therapy in refractory neuroblastoma. *J Clin Oncol*.

- 2007;25:1054–60. doi:10.1200/JCO.2006.09.3484.
44. Michelmore A, Gong WQ, Jenkins P, Ralston J. The interaction of linear polyphosphates with titanium dioxide surfaces. *PCCP Phys Chem Chem Phys*. 2000;2:2985–92. doi:10.1039/b001213k.
45. Misra R, Sahoo SK. Intracellular trafficking of nuclear localization signal conjugated nanoparticles for cancer therapy. *Eur J Pharm Sci*. 2010;39:152–63. doi:10.1016/j.ejps.2009.11.010.
46. Nakagawara A, Ikeda K, Tasaka H. Dopaminergic neuroblastoma as a poor prognostic subgroup. *J Pediatr Surg*. 1988;23:346–9. doi:10.1016/s0022-3468(88)80204-5.
47. Nakamura Y, Ozaki T, Niizuma H, Ohira M, Kamijo T, Nakagawara A. Functional characterization of a new p53 mutant generated by homozygous deletion in a neuroblastoma cell line. *Biochem Biophys Res Commun*. 2007;354:892–8. doi:10.1016/j.bbrc.2007.01.057.
48. Ortega R, Bohic S, Tucoulou R, Somogyi A, Deves G. Microchemical element imaging of yeast and human cells using synchrotron X-ray microprobe with Kirkpatrick-Baez. *optics Anal Chem*. 2004;76:309–14. doi:10.1021/ac035037r.
49. Paltiel HJ, Gelfand MJ, Elgazzar AH, Washburn LC, Harris RE, Masters PR, Golsch GJ. Neural crest tumors: I-123 MIBG imaging. in children *Radiology*. 1994;190:117–21. doi:10.1148/radiology.190.1.8259387.
50. Pante N, Kann M. Nuclear pore complex is able to transport macromolecules with diameters of about 39 nm. *Mol Biol Cell*. 2002;13:425–34. doi:10.1091/mbc.01-06-0308.
51. Paulo CS, Pires das Neves R, Ferreira LS. Nanoparticles for intracellular-targeted drug delivery *Nanotechnology*. 2011;22:494002. doi:10.1088/0957-4484/22/49/494002.
52. Paunesku T, et al. Biology of TiO<sub>2</sub>-oligonucleotide nanocomposites *Nat Mater*. 2003;2:343–6. doi:10.1038/nmat875.
53. Paunesku T, et al. Intracellular distribution of TiO<sub>2</sub>-DNA oligonucleotide nanoconjugates directed to nucleolus and mitochondria indicates sequence specificity. *Nano Lett*. 2007;7:596–601. doi:10.1021/nl0624723.
54. Rajh T, Chen LX, Lukas K, Liu T, Thurnauer MC, Tiede DM. Surface Restructuring of Nanoparticles: An Efficient Route for Ligand – Metal Oxide Crosstalk *The Journal of Physical Chemistry B*. 2002;106:10543–52. doi:10.1021/jp021235v.
55. Ryter SW, Kim HP, Hoetzel A, Park JW, Nakahira K, Wang X, Choi AM. Mechanisms of cell death in oxidative stress. *Antioxid Redox Signal*. 2007;9:49–89. doi:10.1089/ars.2007.9.49.
56. Schramm A, et al. Mutational dynamics between primary and relapse neuroblastomas. *Nat Genet*. 2015;47:872–7. doi:10.1038/ng.3349.
57. Stiller CA. Epidemiology and genetics of childhood cancer *Oncogene*. 2004;23:6429–44. doi:10.1038/sj.onc.1207717.
58. Sugiyama M, Seigo K, Hosoya Y, Iguchi A, Manabe A. 131) I-MIBG therapy with WT-1 peptide for refractory neuroblastoma *Pediatrics International: official journal of the Japan Pediatric Society*. 2020;62:746–7. doi:10.1111/ped.14175.

59. Thurn KT, et al. Endocytosis of titanium dioxide nanoparticles in prostate cancer PC-3M cells *Nanomedicine: nanotechnology, biology, and medicine*. 2011;7:123–30. doi:10.1016/j.nano.2010.09.004.
60. Thurn KT, et al. Labeling TiO<sub>2</sub> nanoparticles with dyes for optical fluorescence microscopy and determination of TiO<sub>2</sub>-DNA nanoconjugate stability *Small*. 2009;5:1318–25. doi:10.1002/smll.200801458.
61. Tubiana M. (2005) *Introduction To Radiobiology*. CRC Press. <http://books.google.com/books?id=xiuNc-2H9UEC>.
62. Vo NT, Drakopoulos M, Atwood RC, Reinhard C. Reliable method for calculating the center of rotation in parallel-beam tomography. *Optics express*. 2014;22:19078–86. doi:10.1364/oe.22.019078.
63. Vogt S, Maser J, Jacobsen C. Data analysis for x-ray fluorescence imaging. *Journal De Physique IV: JP*. 2003;104:617–22. doi:10.1051/jp4:20030156.
64. Wang YN, Wang H, Yamaguchi H, Lee HJ, Lee HH, Hung MC. COPI-mediated retrograde trafficking from the Golgi to the ER regulates EGFR nuclear transport *Biochem. Biophys Res Commun*. 2010;399:498–504. doi:10.1016/j.bbrc.2010.07.096.
65. Wang YN, et al. The translocon Sec61beta localized in the inner nuclear membrane transports membrane-embedded EGF receptor to the nucleus. *J Biol Chem*. 2010;285:38720–9. doi:10.1074/jbc.M110.158659.
66. Ward E, DeSantis C, Robbins A, Kohler B, Jemal A. Childhood and adolescent cancer statistics, 2014. *CA Cancer J Clin*. 2014;64:83–103. doi:10.3322/caac.21219.
67. Yoshida GJ. Emerging roles of Myc in stem cell biology and novel tumor therapies. *Journal of experimental clinical cancer research: CR*. 2018;37:173. doi:10.1186/s13046-018-0835-y.
68. Yuan Y, et al. Epidermal growth factor receptor targeted nuclear delivery and high-resolution whole cell X-ray imaging of Fe<sub>3</sub>O<sub>4</sub>@TiO<sub>2</sub> nanoparticles in cancer cells. *ACS Nano*. 2013;7:10502–17. doi:10.1021/nn4033294.
69. Zage PE, et al. UBE4B levels are correlated with clinical outcomes in neuroblastoma patients and with altered neuroblastoma cell proliferation and sensitivity to epidermal growth factor receptor inhibitors *Cancer*. 2013;119:915–23. doi:10.1002/cncr.27785.
70. Zorov DB, Juhaszova M, Sollott SJ. Mitochondrial ROS-induced ROS release: an update and review. *Biochim Biophys Acta*. 2006;1757:509–17. doi:10.1016/j.bbabi.2006.04.029.

## Tables

**Table 1: Cell viabilities in the presence of bare nanocomposites following irradiation**

Fe <sub>3</sub> O <sub>4</sub> @TiO <sub>2</sub>		0 nM	100 nM	250 nM
SK-N-AS	0 Gy	100 ± 2.22	100 ± 2.00	100 ± 1.42
	2 Gy	88.15 ± 2.85	88.10 ± 3.60	82.22 ± 2.50**
	5 Gy	60.00 ± 1.63	59.61 ± 1.73	50.30 ± 4.49**
	10 Gy	38.90 ± 3.16	38.40 ± 4.53	32.35 ± 2.49**
SK-N-DZ	0 Gy	100 ± 7.42	100 ± 9.29	100 ± 1.86
	2 Gy	78.68 ± 2.70	77.00 ± 3.18	74.55 ± 3.18
	5 Gy	52.13 ± 2.46	51.35 ± 2.47	46.89 ± 1.64**
	10 Gy	31.14 ± 2.78	29.01 ± 3.53	25.03 ± 2.05**

Table of cell viabilities (expressed as % of non-irradiated treatment control for a given concentration of nanoconjugates, after adjustment for baseline cytotoxicity) for SK-N-AS and SK-N-DZ cells treated with varying concentrations of bare nanocomposites and different doses of ionizing radiation (Figure 5). Entries contain mean ± SD. \*\* <0.01 significance level, \*\*\* <0.001 significance level.

**Table 2: Cell viabilities in the presence of DOPAC-Fe<sub>3</sub>O<sub>4</sub>@TiO<sub>2</sub> nanoconjugates following irradiation**

DOPAC-Fe <sub>3</sub> O <sub>4</sub> @TiO <sub>2</sub>		0 nM	100 nM	250 nM
SK-N-AS	0 Gy	100 ± 5.06	100 ± 4.50	100 ± 10.11
	2 Gy	91.84 ± 5.50	57.60 ± 7.28***	53.50 ± 6.60***
	5 Gy	59.38 ± 4.79	26.40 ± 5.56***	17.94 ± 4.54***
	10 Gy	38.11 ± 2.35	14.53 ± 3.50***	7.58 ± 5.67***
SK-N-DZ	0 Gy	100 ± 10.12	100 ± 9.28	100 ± 17.87
	2 Gy	51.97 ± 4.34	40.35 ± 10.15*	36.83 ± 17.71
	5 Gy	40.06 ± 3.35	27.55 ± 3.86***	20.78 ± 12.76**
	10 Gy	17.52 ± 3.23	8.25 ± 3.84**	5.20 ± 10.43*

Table of cell viabilities (expressed as % of non-irradiated treatment control for a given concentration of nanoconjugates, after adjustment for baseline cytotoxicity) for SK-N-AS and SK-N-DZ cells treated with varying concentrations of DOPAC-nanocomposites combined with varying doses of ionizing radiation, from Figure 5. Entries contain mean ± SD. \* <0.05 significance level, \*\* <0.01 significance level, \*\*\* <0.001 significance level.

# Figures

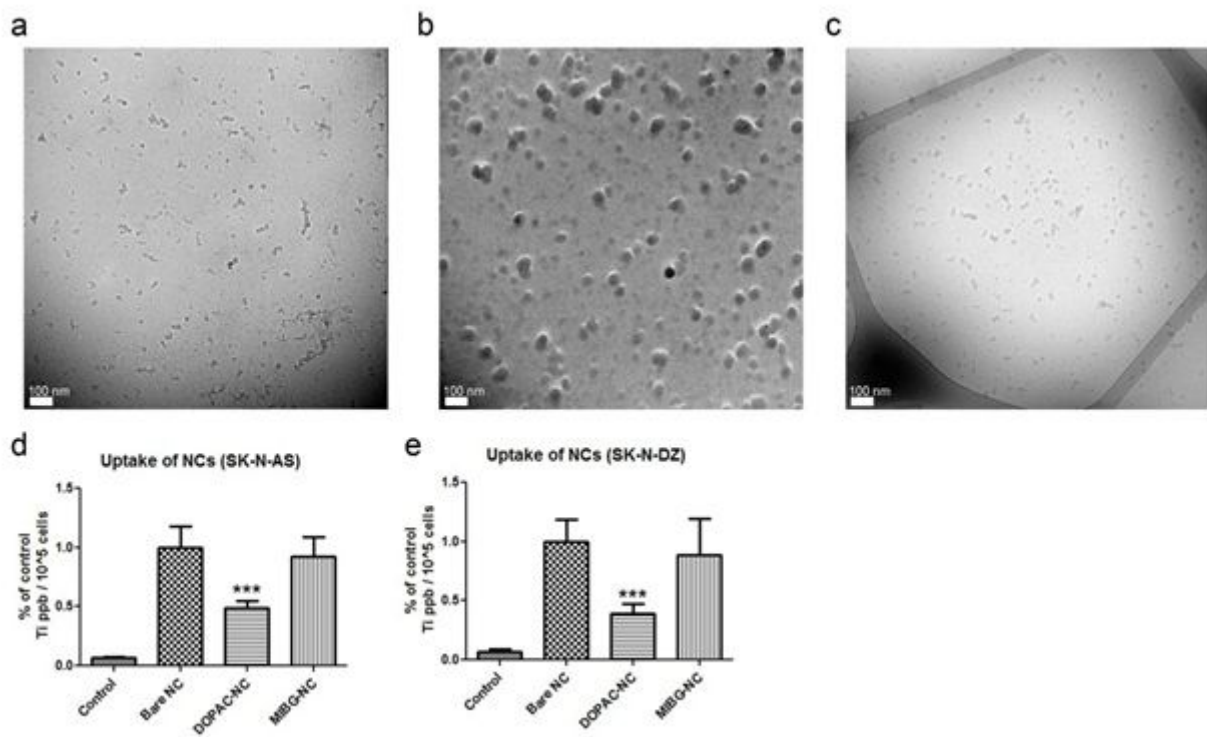
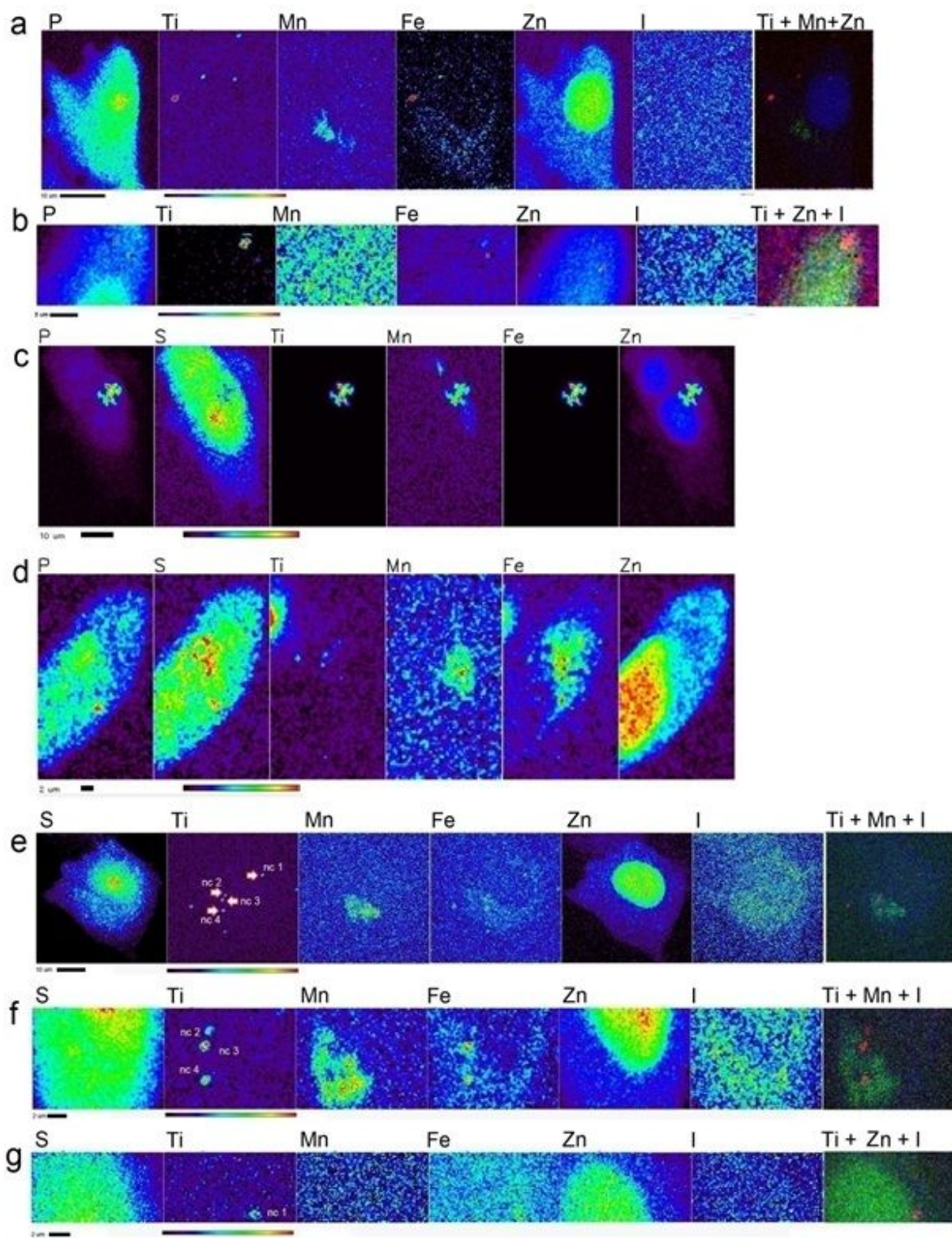


Figure 1

Nanocomposite and nanoconjugate Cryo-TEM show different degrees of aggregation resulting in corresponding differences in nanocomposite uptake by neuroblastoma cells. (a) Cryo-TEM images of bare Fe<sub>3</sub>O<sub>4</sub>@TiO<sub>2</sub> nanocomposites, (b) DOPAC-Fe<sub>3</sub>O<sub>4</sub>@TiO<sub>2</sub> nanoconjugates, and (c) MIBG-DOPAC-Fe<sub>3</sub>O<sub>4</sub>@TiO<sub>2</sub> nanoconjugates mixed with complete cell media, plunge frozen on lacy carbon grids and imaged under cryogenic conditions at 120 kV. For EDS-STEM and IR spectroscopy of nanocomposites see supplemental Figures 1 and 2. d) SK-N-AS cells were treated with 250 nM bare Fe<sub>3</sub>O<sub>4</sub>@TiO<sub>2</sub> nanocomposites, DOPAC-Fe<sub>3</sub>O<sub>4</sub>@TiO<sub>2</sub> nanoconjugates or MIBG-DOPAC-Fe<sub>3</sub>O<sub>4</sub>@TiO<sub>2</sub> nanoconjugates for 1 hour ( $n = 3$ ), washed and collected after trypsinization. Bar graph shows relative quantity of Ti per 10<sup>5</sup> cells; (e) same work was done with SK-N-DZ cells. The total concentration of Ti (ppb) per sample was evaluated by ICP-MS and adjusted for the number of cells counted prior to sample processing for ICP-MS. The final concentration of Ti per 10<sup>5</sup> cells is expressed as a percentage of bare Fe<sub>3</sub>O<sub>4</sub>@TiO<sub>2</sub> nanocomposite uptake; control value corresponds to Ti background from cells not treated with nanoconstructs. Data presented are an average of at least two independent experiments, each with three biological replicates. Error bars indicate mean  $\pm$  SD. \*\*\* <0.001 significance level.



**Figure 2**

Cryo-XFM imaging of SK-N-AS cells treated with three different nanocomposites a) SK-N-AS cells were treated with 250 nM Fe<sub>3</sub>O<sub>4</sub>@TiO<sub>2</sub> nanocomposites for 1 hour. The distribution of Ti and Fe (as proxy for nanocomposites) in SK-N-AS cells was cytoplasmic or associated with the membrane b) the same cell was imaged after a 45 degree rotation, with all Ti signal separated from the Zn rich area of the nucleus c) SK-N-AS cells treated with DOPAC-Fe<sub>3</sub>O<sub>4</sub>@TiO<sub>2</sub> nanoconjugates showing large aggregates with dense

concentration of Ti and Fe; d) SK-N-AS cells also display punctate pattern of smaller aggregates of nanocomposites apparently co-localizing with Mn and Zn signal. e) SK-N-AS cells treated with MIBG-Fe3O<sub>4</sub>@TiO<sub>2</sub> nanoconjugates. Some co-localization of Ti and Fe puncta with Mn and Zn is observed, indicating either potential mitochondrial or nuclear distribution of MIBG-Fe3O<sub>4</sub>@TiO<sub>2</sub> nanoconjugates. f) After a +60 degree rotation, image of the lower portion of same cell is still indicating Ti and Mn co-localization for aggregates nc 3 and nc 4; g) scan of the upper portion of the same cell after a -60 degree rotation suggests that aggregate nc1 is in fact immediately above the nucleus. Scale bar and elemental concentration indicator (black – no signal to red – highest signal) are located under each image.

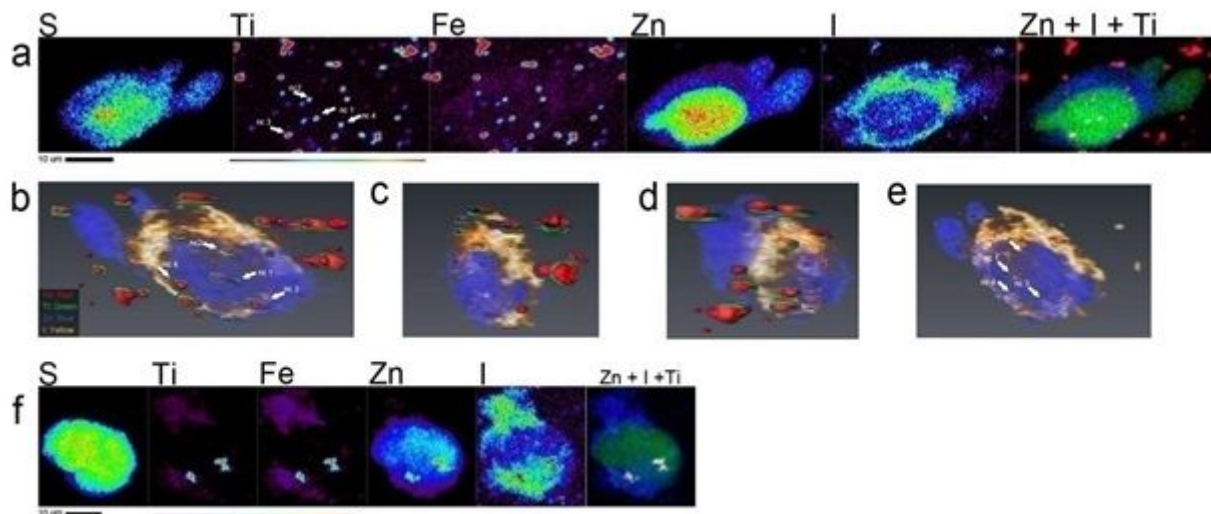


**Figure 3**

Tomographic imaging of targeted MIBG-Fe3O<sub>4</sub>@TiO<sub>2</sub>-B-loop nanoconjugates by Cryo-XFM and tomography indicates partial nuclear localization of the nanoconjugates. a) A single XFM projection of a SK-N-AS cell treated with a 60  $\mu$ M equivalent treatment of MIBG-Fe3O<sub>4</sub>@TiO<sub>2</sub>-B-loop nanoconjugates indicates extensive cytoplasmic and nuclear accumulation of nanoconjugates. Scale bar and elemental concentration indicator (black – no signal to red – highest signal) are located under image. Co-localization image: Blue: iodine, Red: Ti, Green: Zinc (overlapping color for all three elements is white). b-d) Screen captures of different single angle projections of the tomographic reconstruction of the cell seen in a). Different rotation projections confirm the localization of Ti and Fe in the nucleus. e) Rotation projection focused on the iodine signal (indication of MIBG) correspond to the same locations in the cell nucleus seen in b). f) SK-N-DZ cell treated with MIBG-Fe3O<sub>4</sub>@TiO<sub>2</sub>-B-loop nanoconjugates, also suggesting nuclear localization of I and Ti.

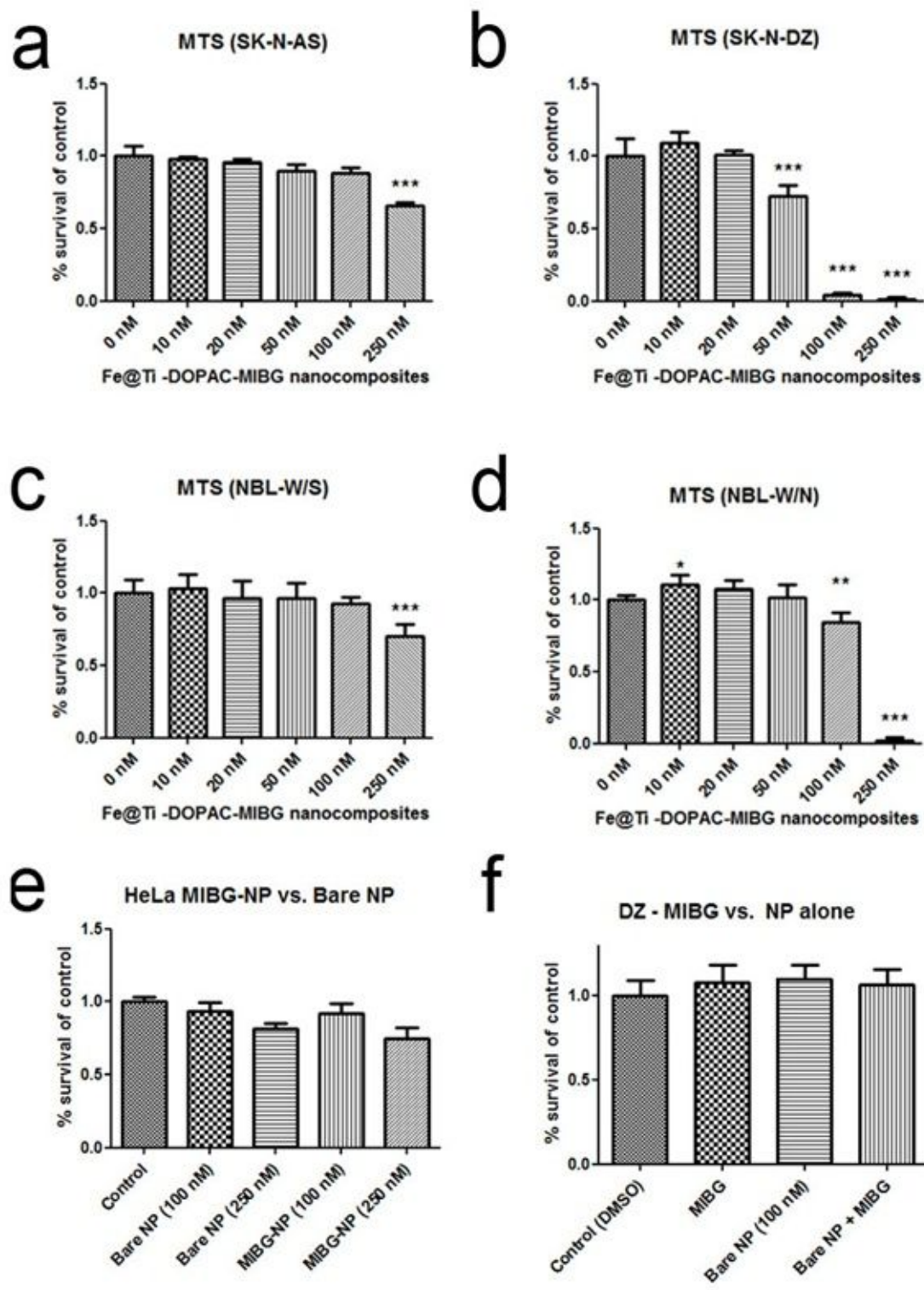


**Figure 4**

Effect of MIBG nanoconjugates on neuroblastoma cell viability (a) SK-N-AS cells; (b) SK-N-DZ; (c) NBL-W/S and (d) NBL-W/N were treated with varying concentrations of Fe<sub>3</sub>O<sub>4</sub>@TiO<sub>2</sub>-MIBG nanoconjugates. Loss of viability was observed by MTS assay as detailed. (e) HeLa cells treated with 100 nM or 250 nM Fe<sub>3</sub>O<sub>4</sub>@TiO<sub>2</sub> bare nanocomposites or MIBG nanoconjugates. (f) SK-N-DZ cells treated with free MIBG (9.3 μM), Bare nanocomposites (100 nM), or bare nanocomposites + free MIBG. No decrease in cell

viability was found in either treatment condition \* : $<0.05$  significance level, \*\*:  $<0.01$  significance level, \*\*\*  $<0.001$  significance level. Datapoints presented are an average of 5 biological replicates. Error bars indicate mean  $\pm$  SD.

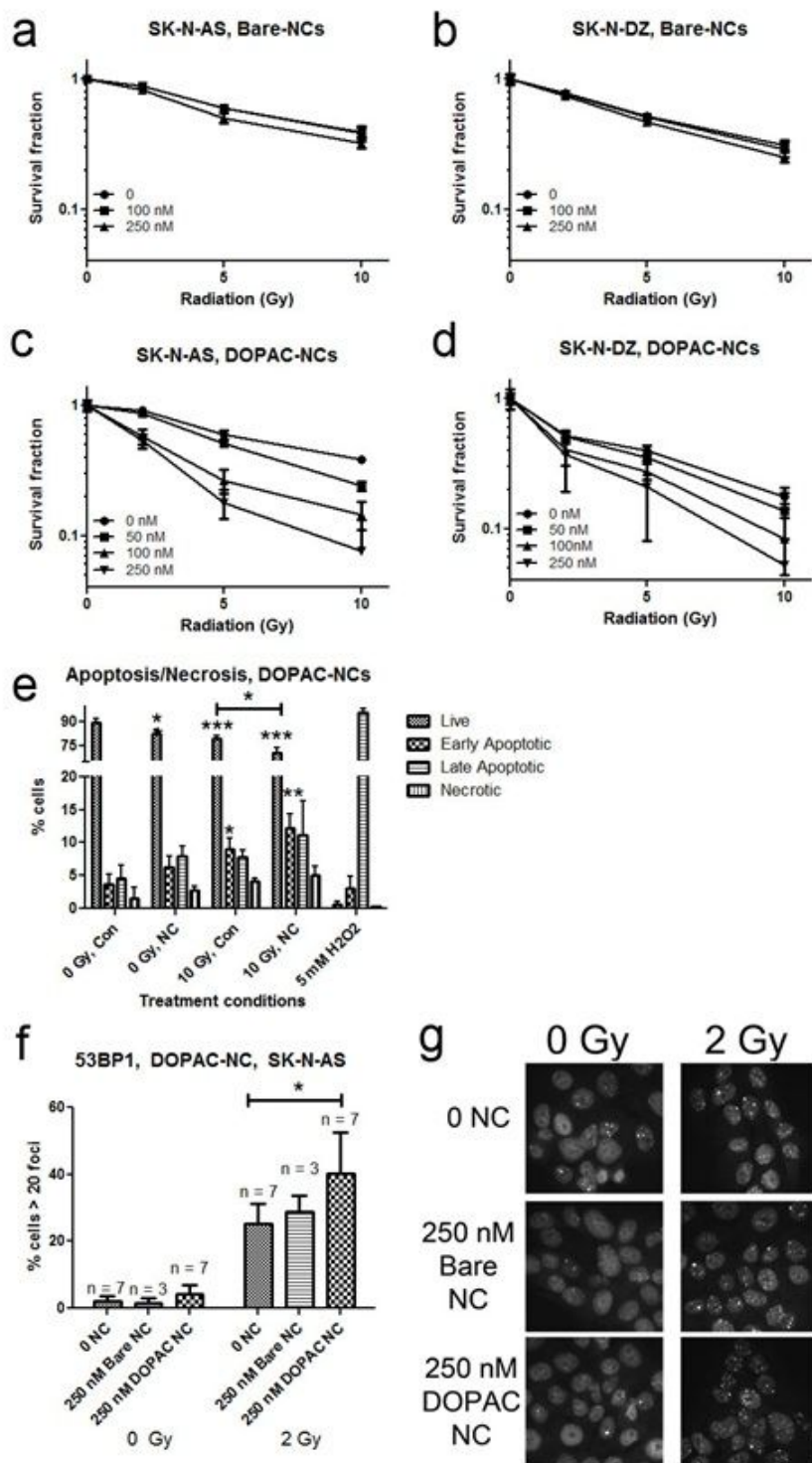


**Figure 5**

Radiosensitizing effects of bare nanocomposites and DOPAC coated nanoconjugates (a,c) SK-N-AS and (b,d) SK-N-DZ cells were irradiated in the presence of bare (Bare-NCs) or DOPAC coated (DOPAC-NCs)

nanoconstructs of different concentrations. Curves were generated by adjusting cell viabilities to 100% for non-irradiated cells in each nanoconstruct treated group. A statistically significant radiosensitizing effect was observed at 250 nM bare nanocomposites in both cell lines, particularly at 10 Gy. Datapoints presented are average of 5 biological replicates and are representative of at least two independent MTS experiments. Error bars indicate mean  $\pm$  SD. e) Annexin V/propidium iodide flow cytometry assay of SK-N-AS cells 24h after irradiation (0 or 10 Gy) preceded by treatment with 250 nM DOPAC-nanocomposites. H<sub>2</sub>O<sub>2</sub> was the positive control. Three independent experiments were done, with 3 biological replicates per experiment. Con = cells not exposed to nanoconjugates; NC = DOPAC nanoconjugate treatment; f) percentage of SK-N-AS cells with >20 foci per nucleus, for untreated or treated with 250 nM bare nanocomposites or 250 nM DOPAC-nanoconjugates for one hour and irradiated as indicated. 53BP1 foci were stained by immunocytochemistry while the nuclei were counter-stained with propidium iodide (PI). At least 100 cells were counted for each treatment group per replicate. N = total number of biological replicates from 4 independent experiments of 1-2 replicates each. There was a significant increase in the percentage of cells with >20 foci after 2 Gy treatment. g) Representative images of cells shown in f). Error bars indicate mean  $\pm$  SD. \* $<0.05$  significance level, \*\*  $<0.01$  significance level, \*\*\*  $<0.001$  significance level when treatment sample is compared to untreated and/or unirradiated control.

## Supplementary Files

This is a list of supplementary files associated with this preprint. Click to download.

- [Graphicalabstract.docx](#)
- [SupplementaryVideo.mpg](#)
- [WillSupplemental.docx](#)